Senior Thesis:

Magnetic Anisotropy in Mixed Chromium Trihalides $CrCl_{3-x}Br_x$

RuiXi Seet[1]

[1] *Department of Physics, Brown University, Providence, Rhode Island 02912, USA*

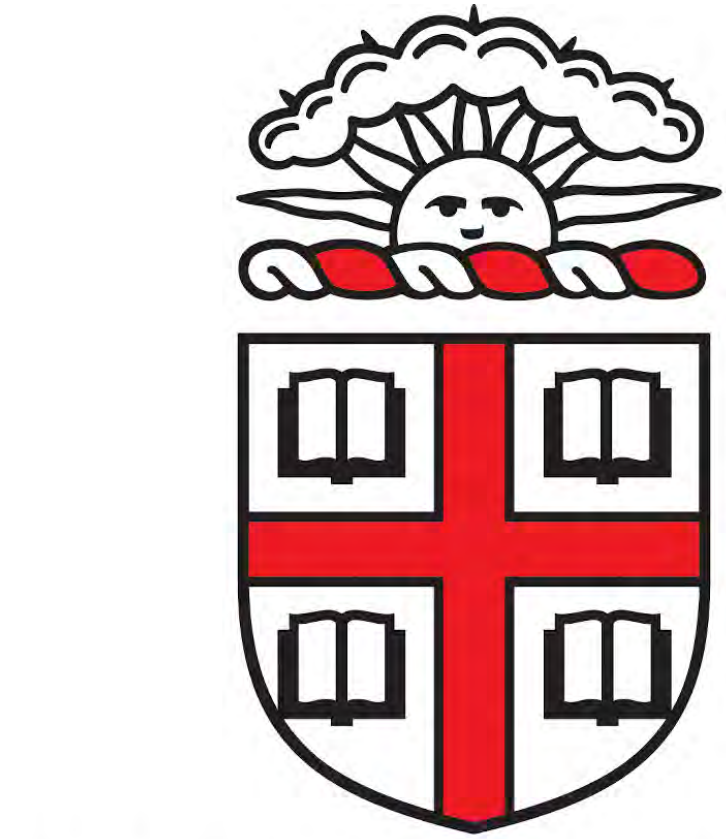

BROWN

Submitted in partial fulfillment of the Honors requirements for the degree of Bachelor of Science in Physics of the Diploma of Brown University in May 2020 under the guidance of Prof. K. Plumb

ABSTRACT

In this thesis, I explore phase inhomogeneity in mixed halide compounds through x-ray diffraction measurements of Bragg peaks in a single-crystal. Using prior knowledge of the properties of transition metal trihalides, transition metal trihalides made of mixed halides were studied using an X-ray diffractometer. In particular, the compound of interest is chromium trichloride ($CrCl_3$) mixed with bromine: $CrCl_{3-x}Br_x$, where x is the amount of Br (the heavier halide) mixed with Cl (the lighter halide) in the transition metal trihalide compound. To ensure a wide range of temperature, a cryostat setup was used for low temperature measurements and a furnace assembly was designed and machined for high temperature (up to 420K) measurements. Temperature dependent X-ray diffraction measurements were taken and subsequently, 2θ, d-spacing and peak width against temperature were plotted to investigate structural changes in the sample crystal. The X-ray diffraction measurement of structural changes is instrumental in investigating phase inhomogeneity: if the mixed chromium trihalide compound is homogeneous, only one structural transition should occur. However, should multiple structural transitions occur at different temperatures, it would indicate that the mixed chromium trihalide compound is in fact a material with inhomogeneous phases. Thus, the use of X-rays as a probe of structural transition in the mixed chromium trihalide enables us to disentangle the disorder from the structural changes that have been introduced. Preliminary results discussed in this thesis suggest a single temperature-induced structural transition at approximately $T = 300$K in a $CrCl_{0.75}Br_{2.25}$ single crystal sample.

ACKNOWLEDGEMENTS

I would like to express my gratitude to the following people for their valuable guidance and help throughout the thesis process - thank you for being generous with your time, energy and knowledge:

- Prof. K. Plumb, for being immensely generous with his guidance throughout the entire senior thesis process,
- T. H. Yang, for being helpful and supportive with carrying out experimental procedures in proxy,
- other members of PlumbLab, for being supportive and providing valuable feedback during the practice of my thesis presentation,
- the Department of Physics, for giving me the academic support for completing my thesis, and
- my family and friends, who were gracious with me despite my disappearing into the lab for many long hours and for being empathetic during times of frustration.

CONTENTS

INTRODUCTION

Magnetic van der Waals (vdW) materials have recently gained interest as potential candidates for two dimensional materials used to study size reduction and efficiency improvement in microelectronics. Additionally, it is desirable to combine functionalities from various devices to improve versatility of electronic devices. For example, in spintronic devices the spin of an electron is used in addition to its charge can dramatically increase the productivity of nanodevices. [1] In particular, graphene, a carbon nanomaterial has been the subject of such 2D electronic materials research. However, transition metal halides have also emerged as a promising candidate because their optical and magnetic properties can be tuned using various chemical paths such as the superexchange path. Chromium trihalides CrX_3 (X =Cl, Br, I) are examples of transition metal halides which are layered and van der Waals (vdW) bonded. CrX_3 compounds are also magnetic, which is an important property for the fabrication of spintronic devices. As chromium trihalides have not been the locus of research attention, they are not well-understood despite having been discovered and known for a long period of time. It is the goal of my senior thesis to explore the structural phase transitions and phase inhomogeneity in mixed chromium trihalides.

Figure 1 illustrates the primary goal of my thesis. In the mixed chromium trihalides, it was proposed that substituting Br for Cl can continuously affect exchange anisotropy. This conclusion was inferred from bulk average measurements and it is also possible that regions of different exchange anisotropy exists in the mixed compound. To resolve this issue, I carried out temperature dependent X-ray diffraction measurements on the single crystal of the mixed compound. The X-ray diffraction measurement of structural changes is instrumental in investigating phase inhomogeneity: if the mixed chromium trihalide compound is homogeneous, only one structural transition should occur. However, should multiple structural transitions occur at different temperatures, it would indicate that the mixed chromium trihalide compound is in fact a material with inhomogeneous phases. Thus, the use of X-rays as a probe of structural transition in the mixed chromium trihalide enables us to disentangle the disorder from the structural changes that have been introduced.

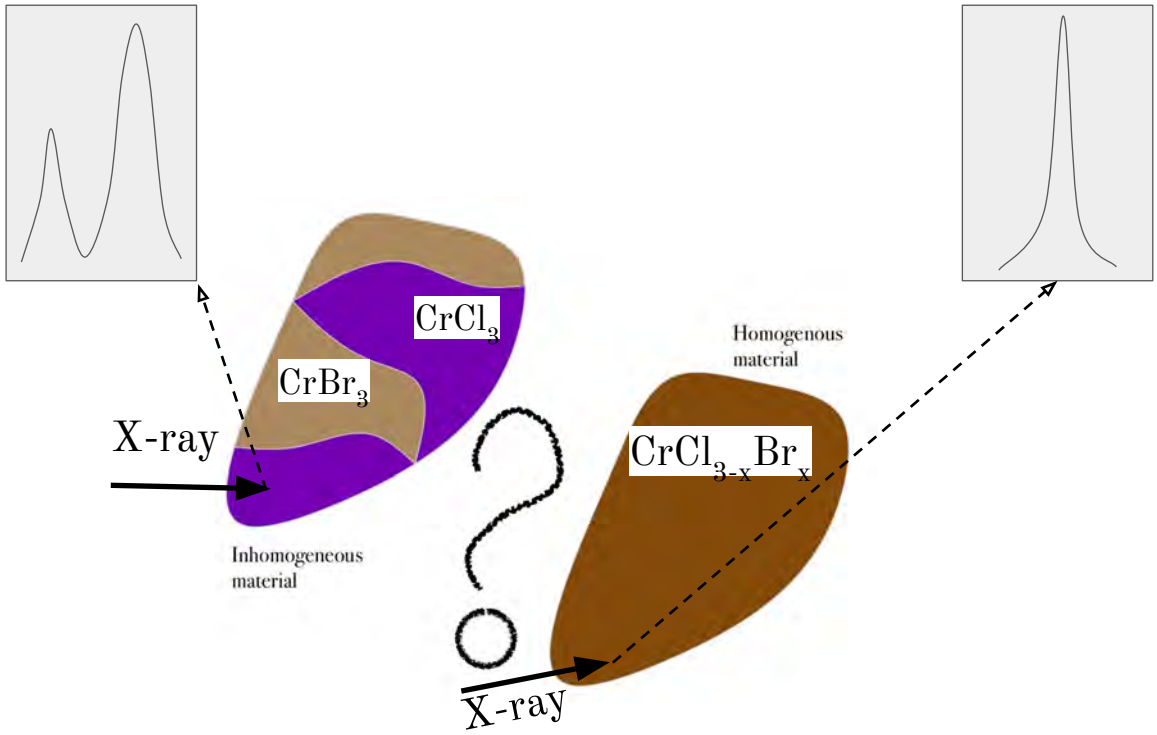

FIG. 1: Simple illustration of the motivation of my senior thesis. X-rays are used to probe the structure of mixed chromium trihalide compounds in order to disentangle disorder from the structural changes introduced from mixing a lighter halide (Cl) with a heavier halide (Br) .

Background Theory

Crystal Structure of Chromium Trihalide

Table 1 shows a summary of the crystal structure information for chromium trihalides and a view of the crystal structure is shown in Fig. 3. They have partially filled d-shells, indicating that magnetism are typically expected in them. This is due to the fact that fully filled shells have magnetic moments that completely cancel each other out, thus only partially filled shells can have an atomic magnetic moment (Fig. 2). As such, we can expect to see magnetic behaviour in atoms with partially filled shells, such as chromium trihalides. $CrCl_3$ and $CrBr_3$ share a similar crystallographic structure: a honeycomb net made of Cr cations sharing edges within an octahedral network. Each Cr cation is surrounded by six Cl/Br anions, making up a single unit of $CrCl_6$. The planar honeycomb layer is formed when each unit share edges to make up the monoclinic octahedral structure. The subsequent layers stack to form the 3D crystal of $CrCl_3$ or $CrBr_3$ (Fig. 4).

Compound	Structure Type	Magnetic Order
$CrCl_3$	Monoclinic C2/m	Antiferromagnetic
$CrBr_3$	Rhombohedral R3	Ferromagnetic
CrI_3	Monoclinic C2/m	Ferromagnetic

TABLE I: Summary of crystal structure information for chromium trihalides.

Crystallographic Structural Transition

Chromium trihalides are known to undergo a structural transition induced by temperature between their respective structure type (C2/m and R3 space groups). The monoclinic C2/m and rhombohedral R3 space group differ mainly in their stacking: the rhombohedral lattice is based on the stacking of hexagonal layers whereas the monoclinic lattice is based on the stacking of oblique/slanting layers [3].

The corresponding temperatures for these transitions according to literature are 240, 420 and and 210K in $CrCl_3$, $CrBr_3$ and CrI_3 respectively[4]. In previous work, CrI_3 has been found to undergo a first-order structural transition (discontinuity in first derivative of free energy) when the crystal is cooled down from room temperature, simultaneously

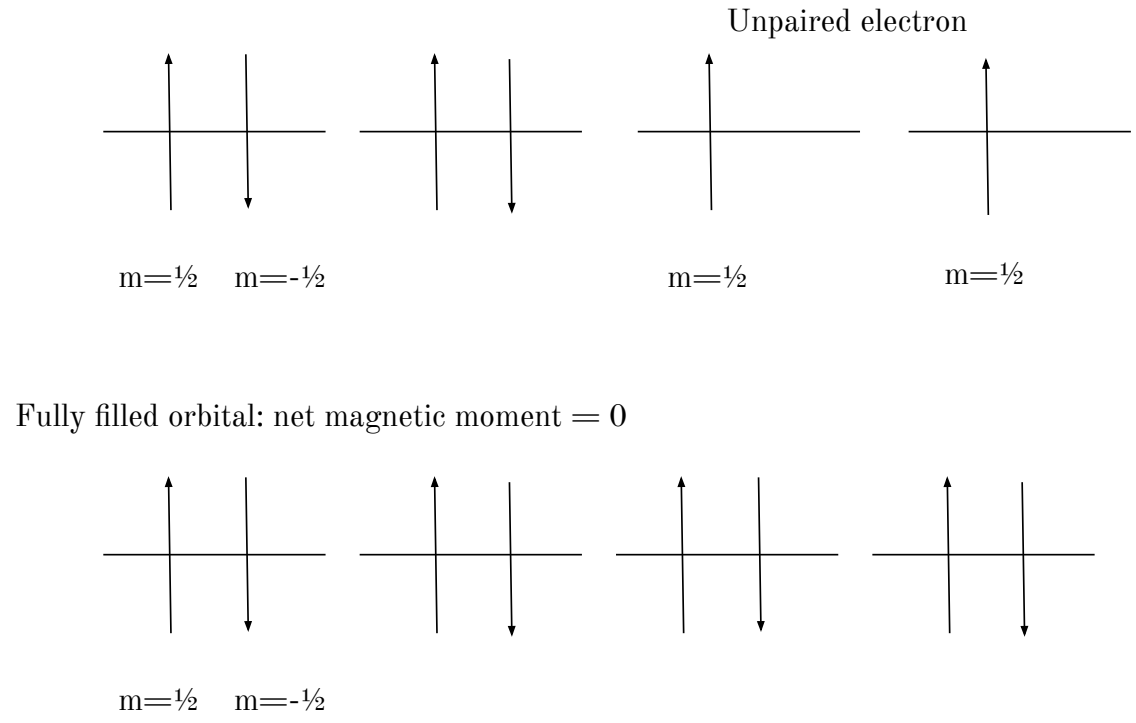

FIG. 2: Figure illustrating difference in net magnetic moment between a fully filled orbital and a partially filled orbital. Fully filled orbitals have magnetic moments that cancel each other out, partially filled shells will have atomic magnetic moment where magnetic moment is expected. The latter is the case for chromium trihalides.

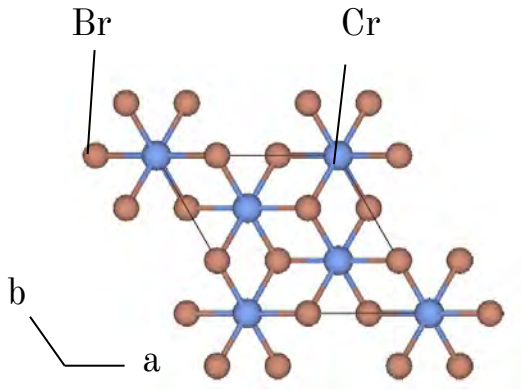

FIG. 3: Visualization of $CrBr_3$ crystal structure from the perspective of the c-plane. The six ions are the Br ions which surround the Cr ion in an edge-sharing octahedral network. Its rhombohedral R3 lattice structure is based on the stacking of hexagonal layers.

demonstrating thermal hysteresis. Over the temperature range of interest, both structural types have been shown to coexist over the range of measured temperature, indicating a

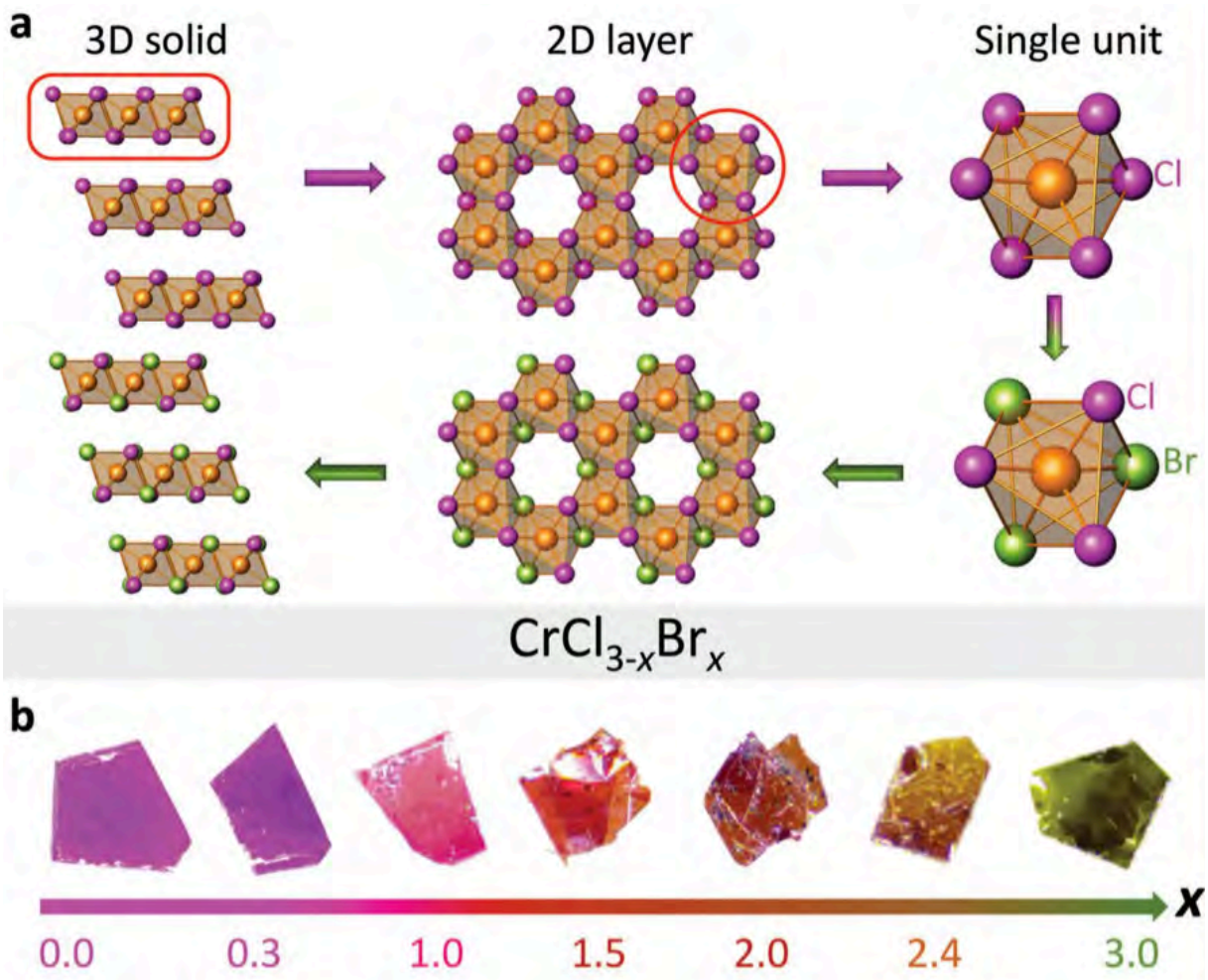

FIG. 4: a) The structure of a chromium trihalide 3D crystal: each Cr ion is surrounded by 6 halide ions forming a honeycomb net of edge-sharing cations in an octahedral network. b) Optical images of $CrCl_{3-x}Br_x$ crystals with increasing x showing a gradual change of color from pink to green.[2]

crystallographic phase transition. As the compound is made of layers that change during the transition, the transition is said to be driven by interlayer interactions.

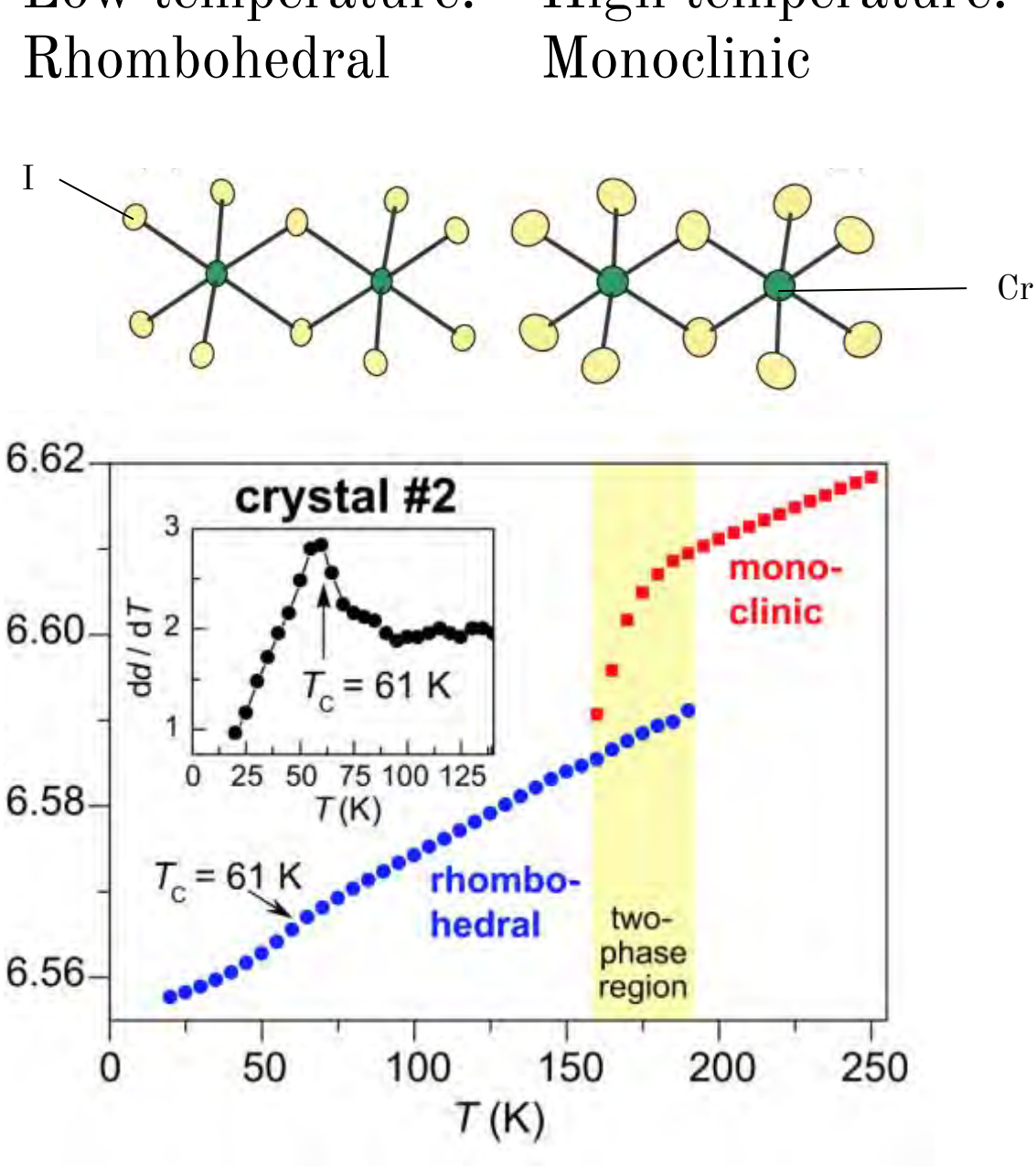

FIG. 5: Experimental result of XRD measurement on 004 peak in a CrI_3 crystal: plot of d-spacing against temperature show the coexistence of the two phase region, indicating crystallographic phase transition between low temperature rhombohedral structure and high temperature monoclinic structure. [4]

Magnetism in an Atom

An electron possesses an intrinsic magnetic moment associated with its intrinsic angular momentum - spin. Going through a similar exercise as before, an electron can only have spin number, $s = \frac{1}{2}$ and possess $2s + 1$ possible angular momentum values, $m_s = \pm\frac{1}{2}$; the component of the angular momentum along an axis is then $\pm\frac{\hbar}{2}$. Analogous to the electronic angular momentum, the magnitude of the spin orbital momentum of an electron is $\sqrt{s(s+1)\hbar} = \frac{\sqrt{3}}{2}\hbar$.

Due to the orbital motion of electrons around the nucleus, electrons possess orbital angular momentum in addition to the electronic angular momentum. Given that the component of the angular momentum along an axis is $m_l\hbar$, the magnitude of the orbital angular momentum along an axis (say the z axis) is then $\sqrt{l(l_1)}\hbar$. As a result, the magnetic moment along the z axis is $-m_l\mu_B$ and magnitude of the total magnetic dipole moment is $\sqrt{l(l+1)}\mu_B$.

Including both spin and orbital components and returning to the relationship between total angular momentum, $j = l + s$ and magnetic moment: the two are related by the magnetic moment component along an axis: $\sqrt{j(j+1)}g\mu_B$, where $g =\approx 2$ is the g-factor and $\mu_B = 9.274 \times 10^{-24}$ J/T is the Bohr magneton.

A simpler physical image of where magnetism comes from is as follows: each unpaired electron possesses a spin which is why they behave like a tiny magnet. For a bulk object to be a magnet, many electrons are required to point their spins in the same direction. In cases where electrons align their spins with each other, it is to reduce their enormous Coulomb repulsion. Additionally, electrons also point their spins in the same direction to obey Pauli's exclusion principle - having the same spins would mean having different locations, which reduces the Coulomb repulsion that exists between electrons placed near each other. It is this saving of energy by aligning spins in a particular direction as a result of reducing Coulomb repulsion and obeying Pauli's principle that is referred to as the exchange interaction.

Exchange Interaction

Essentially, exchange interactions are electrostatic interactions: like charges cost energy if they are close together and save energy if they are far apart. In a simple model with two

electrons, the allowed states are only the symmetrized or anti-symmetrized product states to obey exchange symmetry. In the case of electrons, the overall wave function is asymmetric, implying the following (Eq.1): if the spatial part is symmetric, the spin part must be an anti-symmetric singlet state χ_S (S=0). If the spatial part is asymmetric, the spin part must be a symmetric triplet state χ_T (S=1).

$$\begin{aligned}\psi_s &= \frac{1}{\sqrt{2}}[\psi_a(\mathbf{r}_1)\psi_b(\mathbf{r}_2) + \psi_a(\mathbf{r}_2)\psi_b(\mathbf{r}_1)]\chi_S \\ \psi_t &= \frac{1}{\sqrt{2}}[\psi_a(\mathbf{r}_1)\psi_b(\mathbf{r}_2) - \psi_a(\mathbf{r}_2)\psi_b(\mathbf{r}_1)]\chi_T. \end{aligned} \tag{1}$$

with the associated energies $E_S = \int \psi_S^* \hat{\mathcal{H}} \psi_S d\mathbf{r}_1 d\mathbf{r}_2$ and $E_T = \int \psi_T^* \hat{\mathcal{H}} \psi_T d\mathbf{r}_1 d\mathbf{r}_2$ (assuming χ_S and χ_T are normalized). Making use of spin vectors $\mathbf{S}_{1,2}$, we can parametrize $E_S - E_T$: for a singlet state $\mathbf{S}_1 \cdot \mathbf{S}_2 = \frac{3}{4}$ and $\mathbf{S}_1 \cdot \mathbf{S}_2 = \frac{1}{4}$ for a triplet state. Thus, the effective Hamiltonian comprises a constant term and a spin dependent term:

$$\mathcal{H} = \frac{1}{4}(E_S + 3E_T) - (E_S - E_T)\mathbf{S}_1 \cdot \mathbf{S}_2. \tag{2}$$

Introducing $J = \frac{E_S - E_T}{2}$, the exchange constant allows a further simplification of the spin dependent term:

$$\hat{\mathcal{H}}^{spin} = -2\mathbf{S}_1 \cdot \mathbf{S}_2 \tag{3}$$

.

Generalizing the two electron model to a many body system a non-trivial feat, but even in the early days of quantum mechanics it was postulated that interactions in Eq. 3 was likely to exist between neighbouring atoms, motivating the Hamiltonian in the Heisenberg model.

$$\mathcal{H} = -\sum_{ij} J_{ij} \mathbf{S}_i \cdot \mathbf{S}_j, \tag{4}$$

where $J_{i,j}$ is the exchange constant between the i^{th} and j^{th} spins.

Superexchange

Superexchange can be found in some ionic solids: it is an indirect exchange interaction between two non-neighbouring magnetic ions mediated by a non-magnetic ion. For example, in $CrCl_3$, the chromium atoms are connected by chloride atoms (Fig. 4a). When the system is perfectly ionized, each chromium ion will have an unpaired electron in the d orbital and the chloride ion will have three unpaired electrons in the p orbital. Assuming that the magnetic moment arises from the single unpaired electron in Cr, antiferromagnetic coupling lowers the kinetic energy of the system by delocalizing the electrons, hence superexchange has a kinetic energy advantage.

Ferromagnetic superexchange exists as well, for example between an oxygen ion between an occupied e_g orbital on a magnetic ion and an unoccupied e_g orbital on a magnetic ion. If the e_g electrons hop unto the unoccupied orbital with a spin aligned to the t_{2g} electrons, there will be an energetic advantage and the superexchange would be ferromagnetic.

Anisotropic exchange interaction

Similar to superexchange interactions, a magnetic ion can possess spin-orbit interaction that couples spin and orbital angular momentum, imparting a spatial anisotropy on exchange interactions. An important example of this is the Dzyaloshinsky-Moriya interaction which acts between two spins $\mathbf{S}_1$ and $\mathbf{S}_2$ leading to the following term in the Hamiltonian:

$$\hat{\mathcal{H}}_{DM} = \mathbf{D} \cdot \mathbf{S}_1 \times \mathbf{S}_2. \tag{5}$$

Generally, $\mathbf{D}$ lies either parallel or perpendicular to the line connecting $\mathbf{S}_1$ and $\mathbf{S}_2$, which will be further explained in the section *Magnetic Anisotropy*[5].

Another anisotropy that arises from λ is the single ion anisotropy. Single ion anisotropy describes the effect of the crystal field: there exists an energetic preference for the spin to align along a particular direction due to the crystal field [5]. Effectively, the interaction of the spin with the crystal field in a crystal is the interaction between the orbital state of a magnetic ion and the surrounding crystal field, which depends on the orientation of the magnetic field. The corresponding term in a Hamiltonian for a uniaxial crystal (energy is only dependent on angle between spin and a particular axis of crystal) is:

$$H_{SI} = -DS_z^2, \tag{6}$$

where D is an anisotropy constant.

Finally, drawing on the theory of exchange interactions, the full Hamiltonian of the spin-wave model is as follows:

$$\hat{\mathcal{H}} = -A\sum_i (S_i^z)^2 - J\sum_{ij} \mathbf{S}_i \cdot \mathbf{S}_j - \lambda \sum_{ij} S_i^z S_j^z, \tag{7}$$

where the first term is the single-ion anisotropy term, the second term, the Heisenberg term is proportional to the d-p orbital overlap and the third term, the anisotropic exchange term is proportional to the strength of the spin-orbit coupling in a compound.

Dimensional Dependence of Magnetic Interaction

Magnetic Anisotropy

I now discuss the consequences of anisotropic interactions in experiments. In the study of 2D materials, magnetic anisotropy is the key parameter to sustain ferromagnetism, the mechanism by which materials are attracted to magnets. Magnetic anisotropy is the tendency of of spins to align in a certain direction and the result of different exchange interactions competing with each other (Eq. 7). In a layered material, the system is said to have a perpendicular or out-of-plane easy axis for magnetization if it is energetically favourable for the spins to be perpendicular to the plane of the material (Fig. 6a), i.e. it possesses Ising anisotropy. [5] If it is energetically more favourable for the spins to be parallel to the plane of the material, then the system is said to have an easy plane (Fig. 6b), corresponding to the XY model.

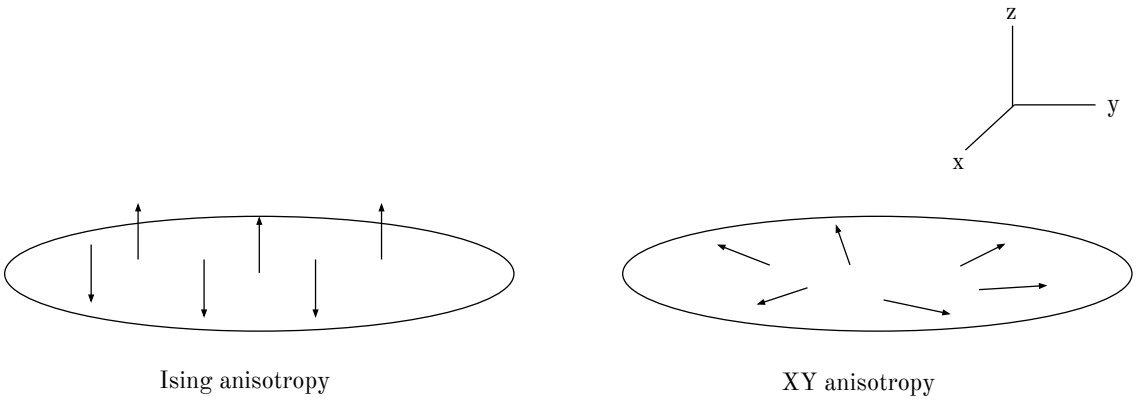

FIG. 6: a) Illustration of Ising anisotropy: it is energetically more favourable for spins to align perpendicular to the plane of the material. b) Illustration of XY anisotropy: it is energetically more favourable for spins to align within the plane of the material.

According to the Mermin-Wagner-Berezinskii theorem, magnetic ordering is not allowed to exist in two-dimensional systems with a continuous symmetry and isotropic, short-ranged magnetic interactions. This is because the integral in Eq. 7, where $n_{magnons}$ is the number of magnon (bosons with spin = 1) modes excited at temperature T, diverges. Calculating the magnon modes requires integrating the magnon density of states multiplied by Bose factor over all frequencies:

$$n_{magnons} = \int_0^\infty \frac{g(\omega)d\omega}{exp(\hbar\omega/k_BT) - 1} \tag{8}$$

where $g(\omega)$ is the density of states over the frequency range, $k_B = 1.380649 \times 10^{-23}$ J/K is the Boltzmann's constant and $\hbar = 1.054571817 \times 10^{-34}$ J $\cdot$ s is the Planck's constant .

The Mermin-Wagner-Berezinskii theorem can be demonstrated by examining deviations of magnetization (Δm) from its maxima in Fourier space [6]:

$$\frac{\Delta m}{2Jns} = \frac{1}{N}\langle s^Z_{tot}\rangle - s = -\frac{1}{N}\sum_k n_k \tag{9}$$

where $n_k = \frac{1}{e^{\omega_k - T} - 1}$ is the average number of excitations for a given k, i.e. decoupled bosons with energy ω_k. Setting the cutoff of $k_0 = \frac{1}{L}$ for a system of length L, taking the assumption

that $\hbar\tilde{\omega} < T < Js$ and using the relation $\hbar\omega_k = 4Js(1-\cos(k))$:

$$\Delta m = -\int_k^{\tilde{k}} dk \frac{k^{d-1}}{(2\pi)^d} \frac{T}{2Jsk^2} - \frac{1}{N}\sum_{k<\tilde{k}} n_k \tag{10}$$

. Eqn. 10 shows a dependence on dimensionality in the first term:

$$\Delta m = \begin{cases} -\frac{T}{2Js}\frac{1}{k_0} & d=1 \\ -\frac{T}{s}\log(\frac{\tilde{k}}{k_0}) & d=2 \end{cases} \tag{11}$$

.

The divergence of the integral in Eqn. 11 show that spontaneous ferromagnetism is impossible and long range order is not permitted in a 2D system possessing continuous symmetry. The Mermin-Wagner-Berezinskii theorem only applies to an isotropic Heisenberg ferromagnet (Fig. 7). Long range excitations (the deviation of spin state from ground state across non-negligible distance) then cost very little energy and the fluctuation of spins can be excited with a small energy cost, where 1D and 2D magnetic order is destroyed by these fluctuations. However, if significant anisotropy exists, then rotating spins from their ground states will cost energy, stabilizing magnetic order in 1D and 2D.

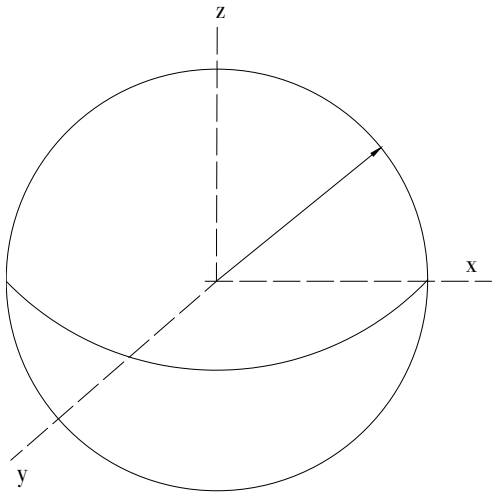

FIG. 7: Semiclassical illustration of spin directions accessible by a Heisenberg ferromagnet: all directions can be accessed without additional energy cost because of the rotational symmetry.

Experimental observations have found two-dimensional ferromagnetic order in monolayers of CrI_3 [4]. The hypothesis is that since CrI_3 is a Van der Waals crystal, given its Van der Waals nature, this magnetic anisotropy can lift the Mermin-Wagner dimensional restriction and stabilize long-range ferromagnetic ordering in a monolayer. [1] This 2D FM ordering is thus attributed to the Ising (out of plane easy axis) anisotropy in CrI_3 and in particular, the spin-orbit coupling of the halide atom along the super-exchange path (Cr-I-Cr). [2] Further, this suggests that the exchange isotropy and the easy axis in chromium trihalides can be controlled by mixing a heavier halide with a lighter one. For example, chromium trichloride ($CrCl_3$) and chromium tribromide ($CrBr_3$) are two chromium trihalides, with Br being the heavier halide compared to Cl. By controlling the SOC in the mixed halide compound $CrCl_{3-x}Br_x$, the magnetic anisotropy can be manipulated as well.

Experimental Observations on Tuning Magnetic Anisotropy in Chromium Trihalides

Drawing from experimental observations of 2D FM ordering in monolayers of CrI_3 [4], further experiments were performed to explore the phenomenon in different mixed chromium trihalides. The paper by Abramchuk et. al. [2] is one of the main motivating studies for my thesis. Different crystals of mixed chromium trihalide compounds,$CrCl_{3-x}Br_x$ [4] were investigated to tune their magnetic and optical properties. A significant result from the paper is shown in Fig. 9.

Fig. 9 shows normalized magnetization M curves plotted as a function of magnetic field measured in 6 samples of $CrCl_{3-x}Br_x$ with increasing Br content, x. In $CrCl_3$, M saturates at a smaller field in $H_\parallel$ (indicating an easy plane, Fig. 8) but the reverse occurs in $CrBr_3$: M saturates at a smaller field in $H_\perp$ (indicating Ising anisotropy 8). The continuous change is highlighted in Fig. 9:g where the difference between the two magnetic fields, $\Delta M = M(H_\parallel) - M(H_\perp)$ is plotted as a function of the magnetic field. Compounds with $x < 2$ exhibit a positive difference ΔM in the positive field direction, corresponding to in-plane easy axis; whereas compounds with $x > 2$ exhibit a positive difference ΔM in the negative field direction, corresponding to an out-of-plane easy axis.

The anisotropy factor $\alpha = \frac{M(H_h)-M(H_e)}{H_e}$ is introduced, where H_h is the magnetization onset of the hard axis and H_e the magnetization onset of the easy axis. By plotting α as a function of x, the Br content, it is shown that the magnetic anisotropy crosses the boundary

between the XY (in-plane easy axis) and Ising (out-of-plane easy axis) limits at $x = 2$.

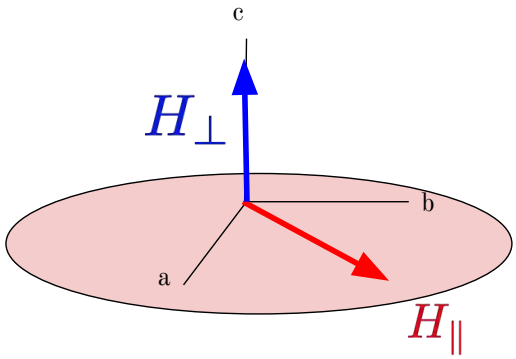

FIG. 8: Legend showing in-plane easy axis and out-of-plane easy axis in $CrCl_{3-x}Br_x$ compounds.

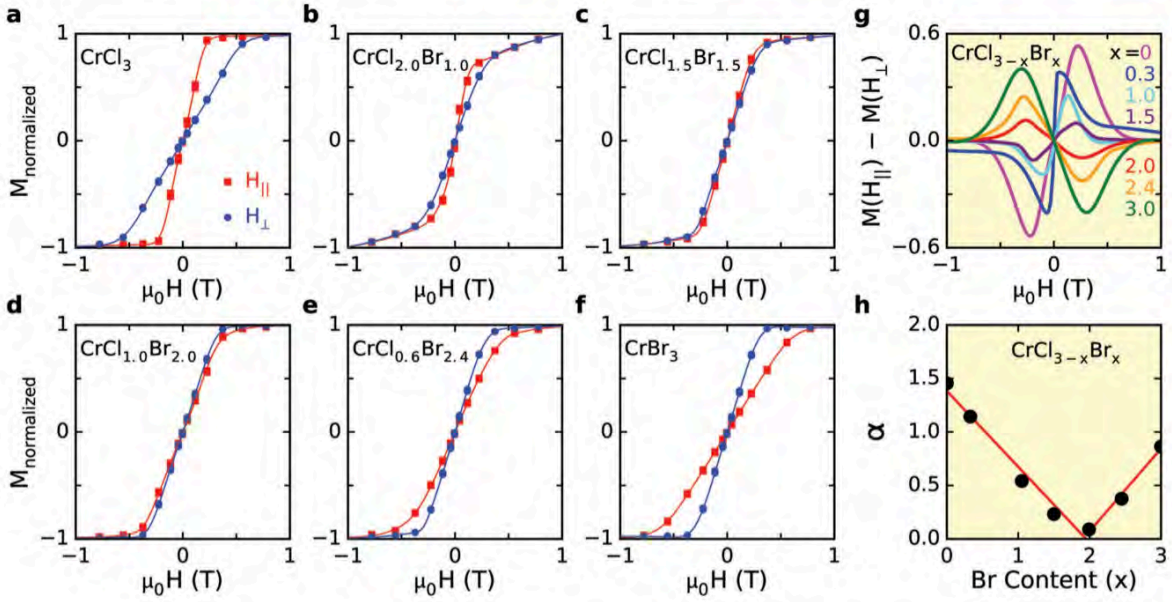

FIG. 9: Figures (a)-(f) show normalized magnetization curves plotted as a function of magnetic field measured in 6 samples of $CrCl_{3-x}Br_x$ with increasing Br content, x. In $CrCl_3$, $H_\parallel$ saturates at a smaller field (in-plane easy axis) but the reverse occurs in $CrBr_3$: $H_\perp$ saturates at a smaller field (out-of-plane easy axis). Fig. (b)-(e) shows that the change occurs gradually across the series. Fig. (g) shows the difference between the $H_\perp$ and $H_\parallel$ fields as a function of magnetic field and Fig. (h) is a plot of the anisotropy factor as a function of Br content. Fig. (g) and (h) show a continuous crossing of the easy axis from in-plane to out-of-plane at $\alpha = 0$ and $x = 2$. [2]

From Eq. 7, the anisotropic exchange term is proportional to the spin-orbit coupling of the compound. In the case of $CrCl_{3-x}Br_x$, Fig. 9 has shown that mixing a lighter halide with a heavier one enhances the SOC along the superexchange path (Cr-X-Cr) when Cl ions are

statistically replaced with Br ions due to the atomic size difference between Cl and Br ions. As there is a strong mixing between Cr d-orbitals and halide p-orbitals in the band structure of chromium trihalides [7][8], the SOC of halides affects Cr d-electrons which are localized by exchange correlations [9]. The anisotropy exchange is tuned as a result of mixing lighter and heavier halides, as shown by the reversal in the anisotropic behaviour in Fig. 9.

Magnetization: an Average Measurement for a Mixed Compound

The motivating hypothesis derived from the paper [2] is that the magnetization measurement in Fig. 9 is an average measurement over a potentially inhomogeneous compound. An average measurement across a non-homogeneous compound might not be representative of the true orientation of the easy axis, as various domains of hard and easy axis might exist (Fig. 1). However, other properties of the mixed compound are sensitive to these different domains, such as the crystallographic structural transition. Here is where X-rays are useful as a probe of these properties: X-ray diffraction measurements of a Bragg peak across a range of temperatures can reveal the occurrence of temperature-induced structural transitions.

X-Ray Diffraction (XRD)

Generally, the X-ray diffraction method refers to the use of X-rays to probe the properties of a sample of interest. The setup of XRD is shown as follows:

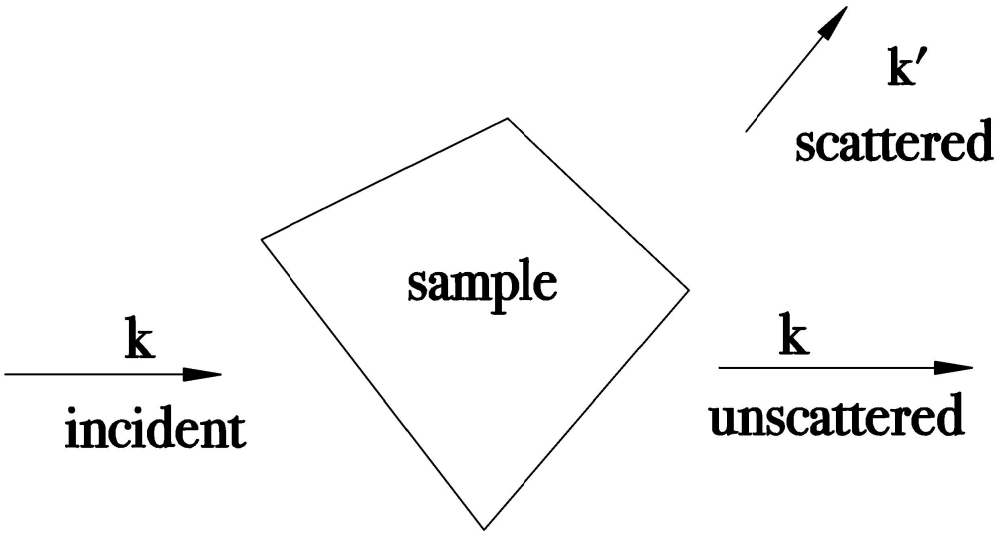

FIG. 10: Geometry of X-ray diffraction measurement. $\mathbf{k}$ represents the incident wave from an elemental X-ray source. $\mathbf{k}$ strikes the sample and as a result, a scattered wave $\mathbf{k}'$ is produced and detected by the detector on the diffractometer.

Conceiving the incident wave as a particle, the sample becomes a potential $V(r)$ which the particle experiences as it passes through the sample. Fermi's golden rule dictates that the transition rate $\Gamma(\mathbf{k}', \mathbf{k})$ per unit time for the particle scattering from k'' to $\mathbf{k}$ is as follows:

$$\Gamma(\mathbf{k}', \mathbf{k}) = \frac{2\pi}{\hbar}|\langle \mathbf{k}'|V|\mathbf{k}\rangle|\delta(E_{k'} - E_k). \tag{12}$$

The matrix element is the Fourier transform of the potential V:

$$\langle \mathbf{k}'|V|\mathbf{k}\rangle = \int \mathbf{dr}\frac{1}{L^3}e^{-i(\mathbf{k}'-\mathbf{k})\cdot\mathbf{r}}V(\mathbf{r}) \tag{13}$$

The exponential term has to vanish except when $\mathbf{k}'-\mathbf{k}$ is a reciprocal vector, i.e. $\mathbf{k}'-\mathbf{k} = \mathbf{G}$. This condition is known as the Laue condition and encapsulates the conservation of crystal momentum. The incident and resulting wave, $\mathbf{k}$ and $\mathbf{k}'$ should also obey the condition $|k| = |\mathbf{k}'|$ to conserve overall energy. The delta function ensures the conservation of energy.

Laue Condition and Bragg Condition

A schematic illustration of the mechanism of Bragg scattering in a crystal or Bragg diffraction is shown in Fig. 11. The incident wave, $\mathbf{k}'$ strikes two layers of atoms (separated by a distance d) and is reflected off the atom. $\mathbf{k}'$ is deflected by 2θ and the extra distance travelled by the wave is $2d\sin\theta$.

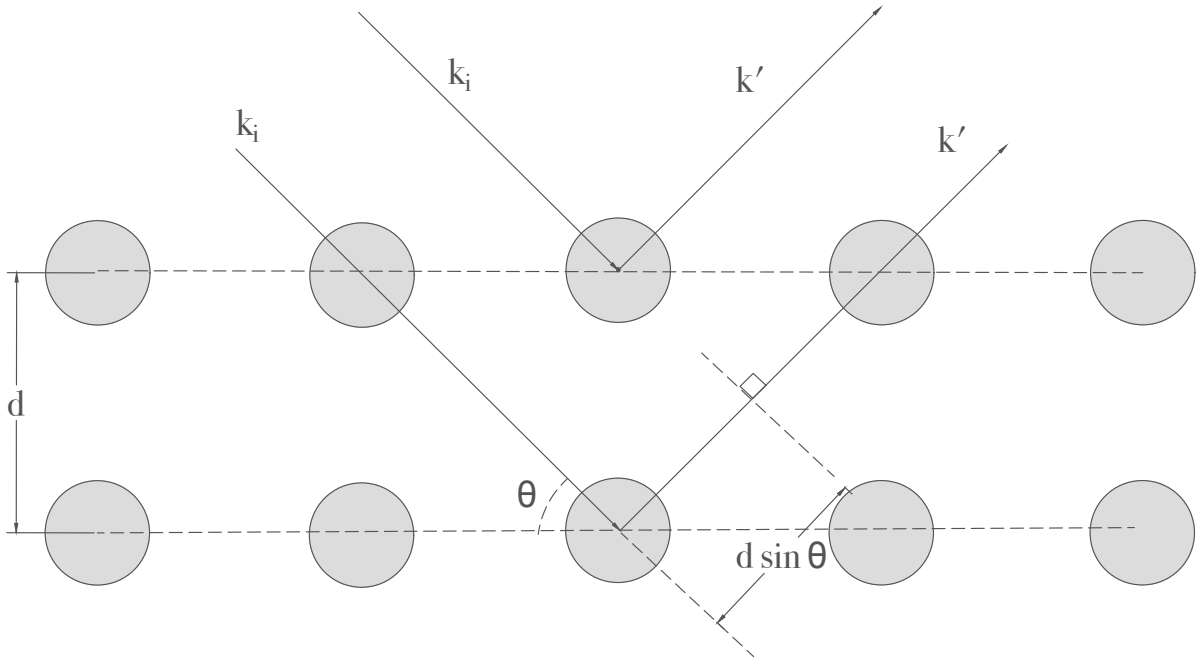

FIG. 11: Bragg scattering geometry.

For constructive interference to occur, the extra distance travelled must be equal to integer number of wavelengths:

$$n\lambda = 2d\sin\theta. \tag{14}$$

The spacing between lattice planes is $d = 2\pi/|\mathbf{G}|$. Fig. 12 shows that $\hat{\mathbf{k}}\cdot\hat{\mathbf{G}} = sin\theta = -\hat{\mathbf{k}'}\cdot\hat{\mathbf{G}}$.

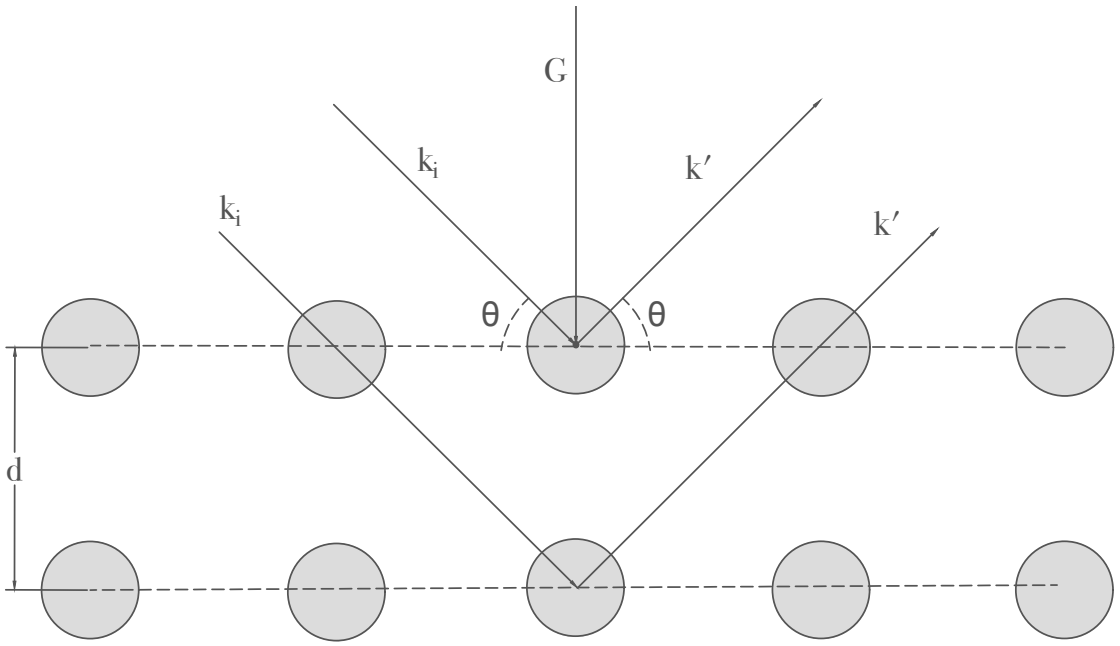

FIG. 12: Laue scattering geometry.

If the Laue condition is satisfied, $\mathbf{k}' - \mathbf{k} = \mathbf{G}$. $|\mathbf{k}|$ as well as $|\mathbf{k}'|$ are then equal to $\frac{2\pi}{\lambda}$, allowing the following reformulation of the Laue condition:

$$\frac{2\pi}{\lambda}(\hat{\mathbf{k}} - \hat{\mathbf{k}}') = \mathbf{G}. \tag{15}$$

Multiplying both sides of the equation with $\hat{\mathbf{G}}$ gives:

$$\begin{aligned} \hat{\mathbf{G}} \cdot \frac{2\pi}{\lambda}(\hat{\mathbf{k}} - \hat{\mathbf{k}}') &= \mathbf{G} \cdot \hat{\mathbf{G}} \\ \frac{2\pi}{\lambda}(\sin\theta - \sin\theta') &= |\mathbf{G}| \\ 2d\sin\theta &= \lambda. \end{aligned} \tag{16}$$

We have recovered the Bragg condition, showing that the Laue condition and Bragg condition are equivalent.

Observing Reciprocal Space

A useful construction for understanding diffraction measurements is the Ewald sphere (Fig. 13). Extending the conception of Fig. 10, the Ewald sphere with radius $r = \frac{1}{\lambda}$ is

a set of possible scattering vectors $\mathbf{k}'$ corresponding to each incoming incident wave $\mathbf{k}$. If $\mathbf{k}'$ lies on the Ewald sphere, then the scattered wave will be visible on the detector. It then follows that rotating the crystal or the incident wave $\mathbf{k}$ through the crystallographic origin will map out a set of possible scattering waves $\mathbf{k}'$ corresponding to reciprocal space, as the sphere moves with the rotation. The new set of scattered waves then describe the relationship between the phase and scatter direction for the incident wave $\mathbf{k}$. Finally, the set of all possible scattered wave vectors is then the reciprocal space.

The reciprocal space is related to the direct space by a set of relations between the lattice vectors $\mathbf{a}, \mathbf{b}, \mathbf{c}$ and the reciprocal lattice vectors $\mathbf{a}^*$,$\mathbf{b}^*$,$\mathbf{c}^*$ to satisfy the Kronecker delta relationship $\mathbf{a} \cdot \mathbf{a}^* = 2\pi\delta$. For example, reciprocal lattice vectors are constructed in the following manner:

$$\mathbf{a}^* = \frac{2\pi \mathbf{b} \times \mathbf{c}}{\mathbf{a} \cdot (\mathbf{b} \times \mathbf{c})} \tag{17}$$

Once vectors have been chosen for a unit cell in direct space ($\mathbf{a}$,$\mathbf{b}$,$\mathbf{c}$), appropriate reciprocal space vectors ($\mathbf{a}^*$,$\mathbf{b}^*$,$\mathbf{c}^*$) can be constructed (Eqn. 17). Miller indices are then used to describe a vector, $\mathbf{G}$ in reciprocal space:

$$\mathbf{G} = h\mathbf{a}^* + k\mathbf{b}^* + l\mathbf{c}^* \tag{18}$$

where hkl are the Miller indices.

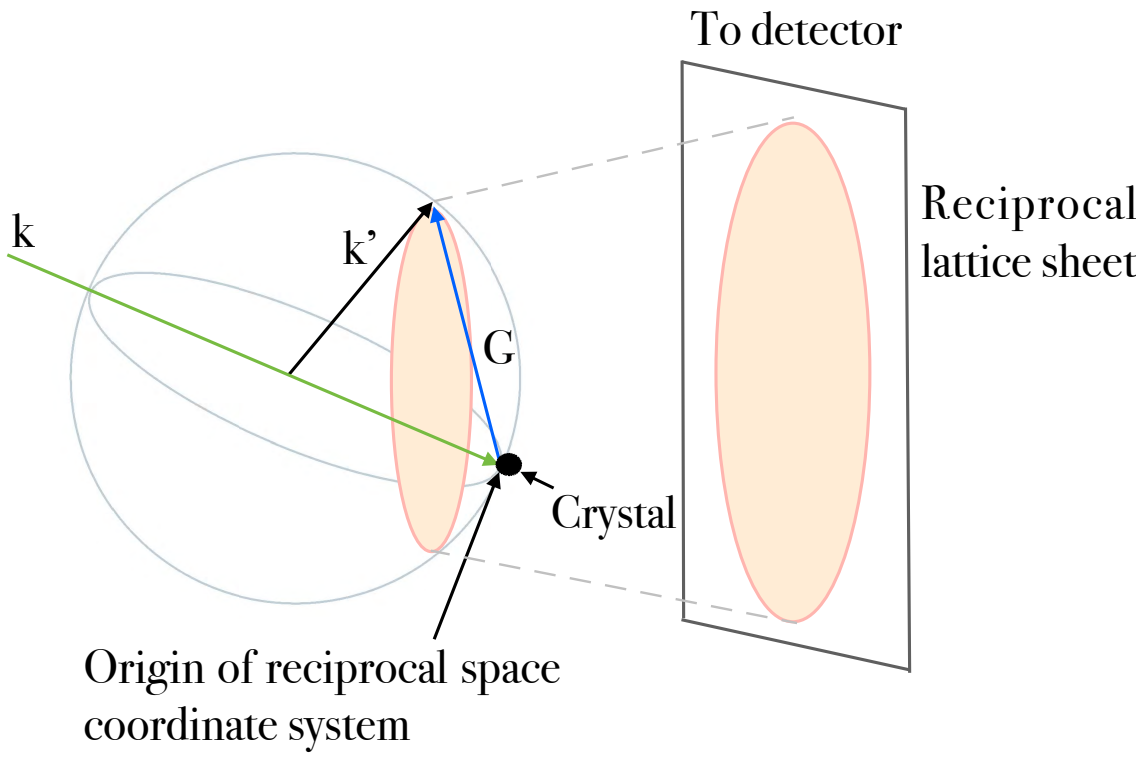

FIG. 13: Ewald sphere showing reciprocal space geometry. $\mathbf{k}'$ represents the diffracted beam and $\mathbf{k}$ the incident beam.

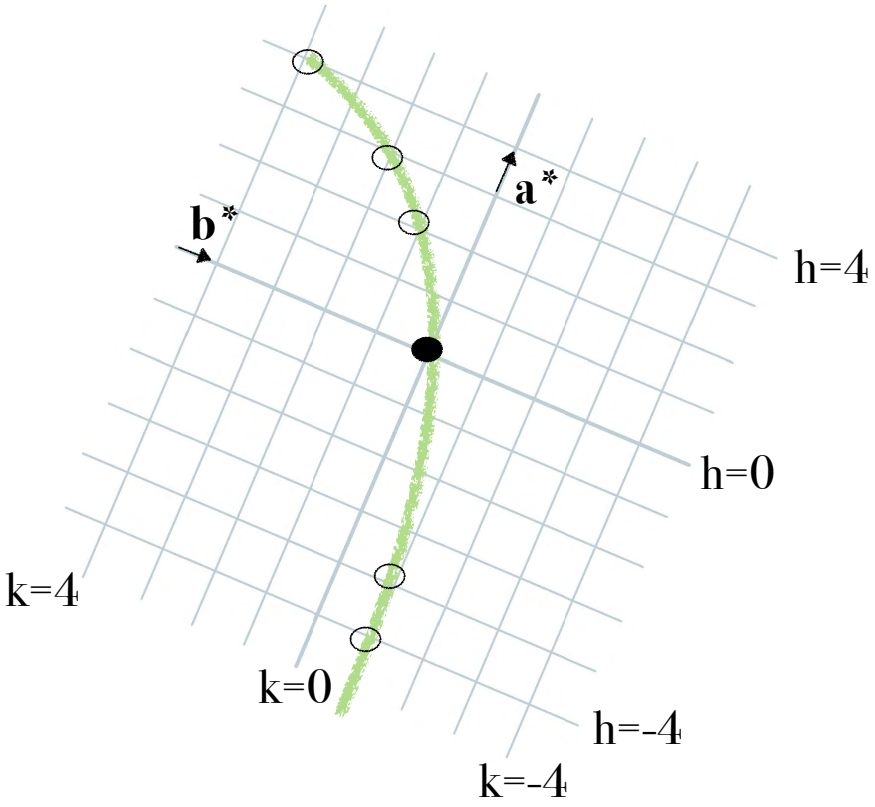

FIG. 14: Ewald sphere showing reciprocal space geometry in a crystal. Reciprocal space is represented by $\mathbf{a}^*$ and $\mathbf{b}^*$, hk indices are Miller indices. The geometry is along the l direction.

Since it is easier to rotate the crystal with respect to the X-ray source rather than the other way around, X-ray diffraction measurements in this experiment are collected by the rotation of the crystal along the ϕ direction at a fixed 2θ value (Fig. 20).

EXPERIMENTAL SETUP

Furnace

As the transition temperature of $CrCl_3$, $CrBr_3$ and CrI_3 range between 230K to 420K, the two temperatures were used as the upper and lower bounds of the experiment to determine the structural transition temperature of the mixed transition metal trihalide. Thus, high temperature XRD measurements were required to probe the temperature dependent structural properties of the $CrCl_{3-x}Br_x$ compound.

In order to accomplish this, a furnace was designed and constructed. The furnace was designed to work in tandem with existing XRD components in the laboratory: for example, the sample post, and the stage where the furnace is placed are designed to be compatible with the X-ray diffractometer. The heater and sensor were selected according to the temperature requirements. A 25Ω100W Lakeshore heater and Platinum RTD $PT103$ temperature sensor with temperature capacity up to 873K were used.

The main design concerns are temperature range (up to 420K at least), heat capacity, and thermal expansion properties. The furnace should be made with material which absorbs heat easily and effectively - low specific heat capacity at 385 J/kg°C. Additionally, the furnace must be made of material that transfers heat effectively: it must possess high thermal conductivity. According to these criteria, we decided that the furnace was to be made out of copper. Copper is also relatively easily malleable and cheap.

As shown in Fig. 15, two holes were made in the curved body of the furnace to house the heater and sensor. Around the perimeter of the furnace, three holes were made to attach the furnace to the shielding stage mechanically. To insulate the screws, a ceramic washer was placed between the screw and the furnace, and the screw was placed in a ceramic sleeve. Further iterations of testing the insulation of the furnace showed that an aerogel insulation sheet was more effective as an insulator than the ceramic washer.

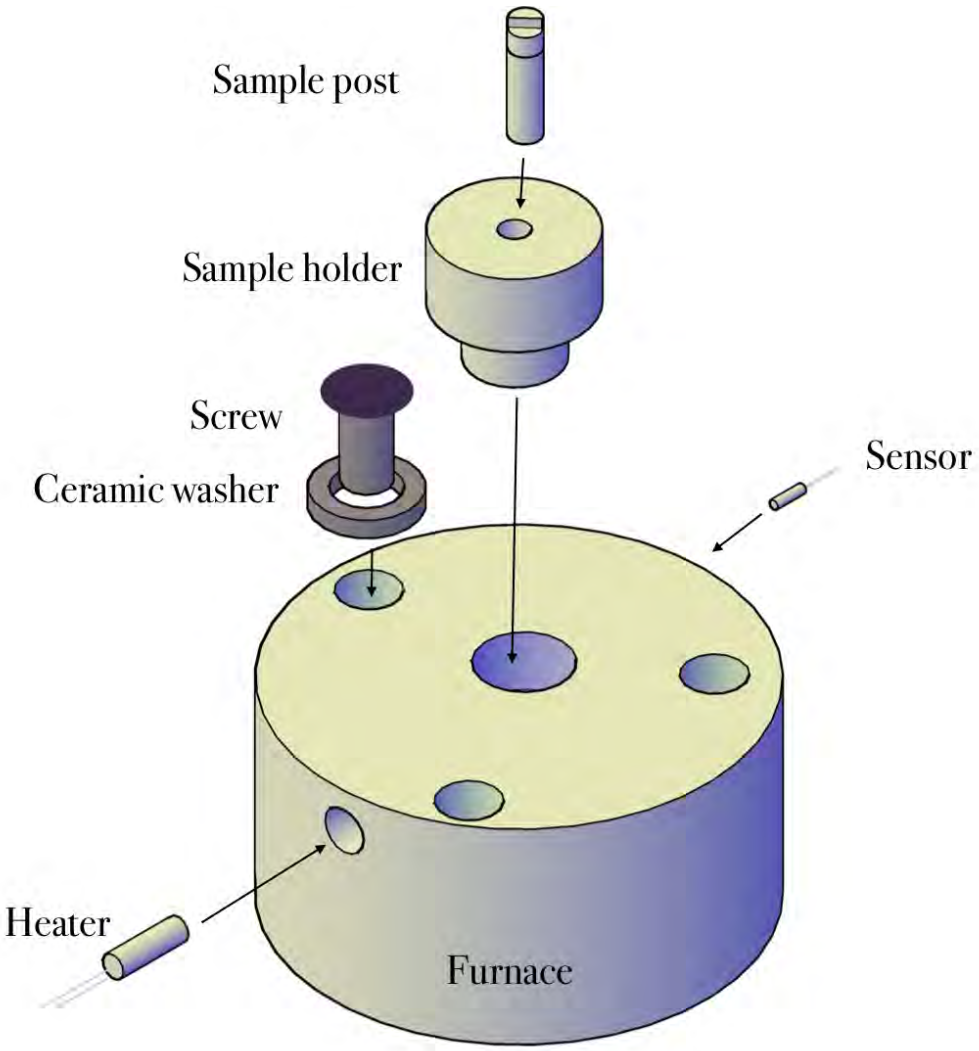

FIG. 15: Main components of furnace setup.

Shielding and Base

Fig. 16 shows the shielding and stage design. In contrast to the furnace, the shielding base and the stage material choice was influenced by thermal insulation capabilities to prevent heat from the furnace from reaching the base. A thermally insulating shielding and base also ensures the heat generated by the heater is retained within the shielding, preventing thermal exchange with the external environment. While aluminium was considered at first, the shielding and base were eventually made out of stainless steel.

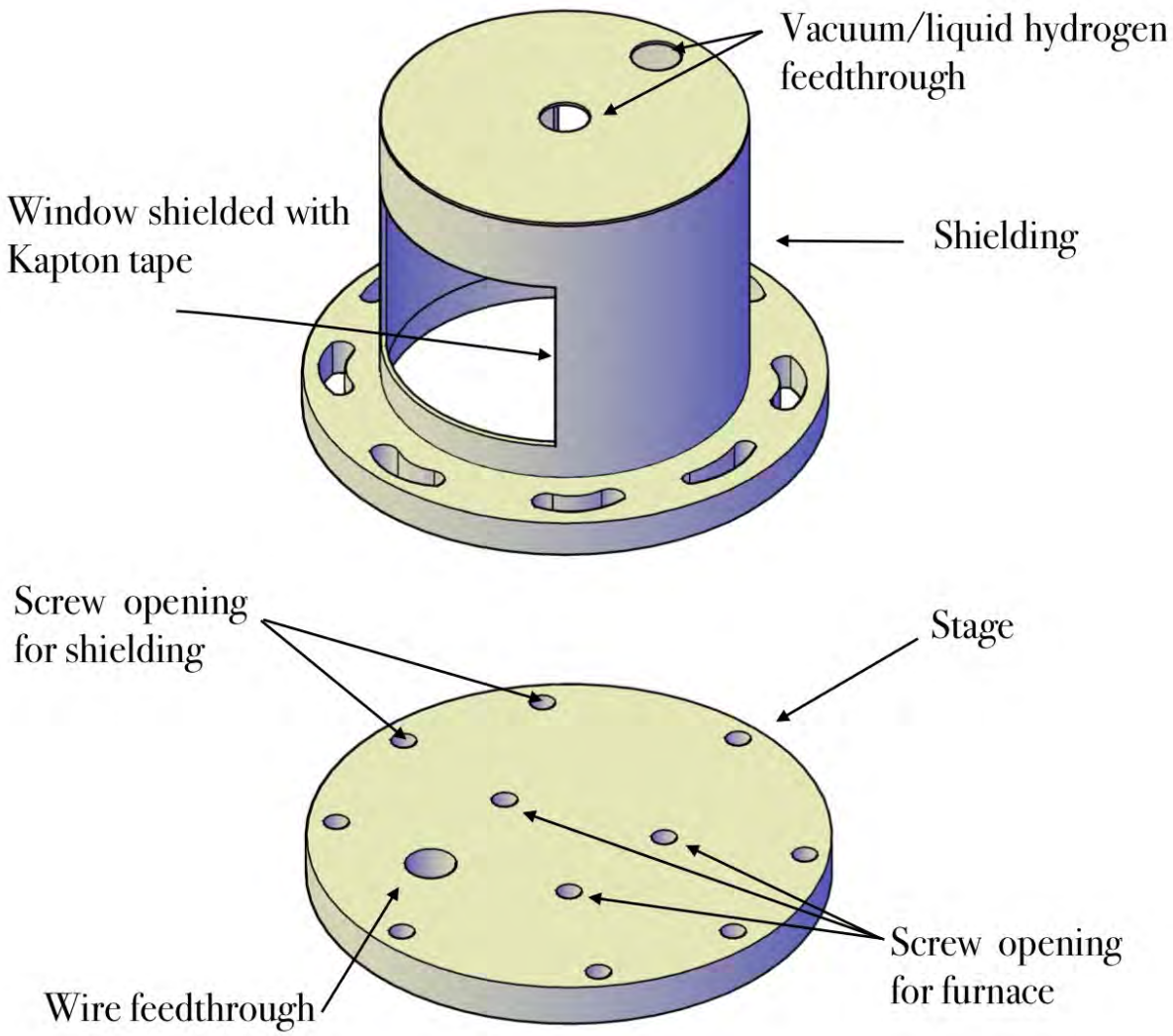

FIG. 16: Main components of shielding and stage. The furnace is attached to the stage and the shielding is attached over the furnace and unto the stage. A window is cut and shielded with Kapton tape to allow X-rays to penetrate the shielding and strike the sample.

Tuning PID Control Loop

P, I, D Terms

With the appropriate heater and platinum RTD sensor connected to the Lakeshore 335 Temperature Controller, the next important calibration is the tuning of the PID control loop. PID is an algorithm in a closed-loop operation. The power output is described by the following equation:

$$Output = P[e + I\int(e)dt + D\frac{de}{dt}] \tag{19}$$

where P is the proportional coefficient, I the integral coefficient and D the derivative coefficient. Error, e is the difference between the temperature setpoint and temperature reading.

Proportional is also known as gain and it is a direct response to the error, $Output(P) = P \cdot e$. Larger proportional gain results in a larger response to error, hence affecting the response rate of the controller to a change. A small gain setting results in an inefficient system which responds slowly to a change, whereas a large gain setting causes the system to respond quickly to a change in setpoint but also is more likely to overshoot the setpoint, which brings us to the next term in the output equation.

The integral term is also known as reset: $Output(I) = PI\int edt$. It is proportional to the duration of the error. Effectively, the integral term sums the total error for a duration of term and multiplies that with the integral coefficient to produce an integral response.

Finally, the derivative term reduces the overshoot and instability that can come from proportional and integral control. $Output(P) = PD\frac{de}{dt}$ shows that the derivative term acts on the change of error with time, as opposed to proportional which is not directly related to the error with respect to time. The derivative control increases the rate at which the temperature approaches setpoint by boosting the output and acts to decrease the overshoot when temperature is near the setpoint by reducing the output, all because it is sensitive to the rate of change of the error.

PID Tuning Method

Tuning the PID control requires each parameter to be tuned independently, starting with P: the term that most strongly influences the output. With I and D set to zero, a small P is applied first to the appropriate heater range (sufficient for the temperature range of interest) and slowly increased until an oscillation of temperature around the setpoint is observed . The proportional value is set to half of the value where oscillation occurs. The period of oscillation τ is then taken and used to determine the integral value: $I = \frac{1000}{\tau}$. This ensures that any offset in temperature is corrected within an appropriate timescale for the system. Finally, the derivative can be increased to reduce the overshoot and increase the rate of dampening of the system to the setpoint (Fig. 17).

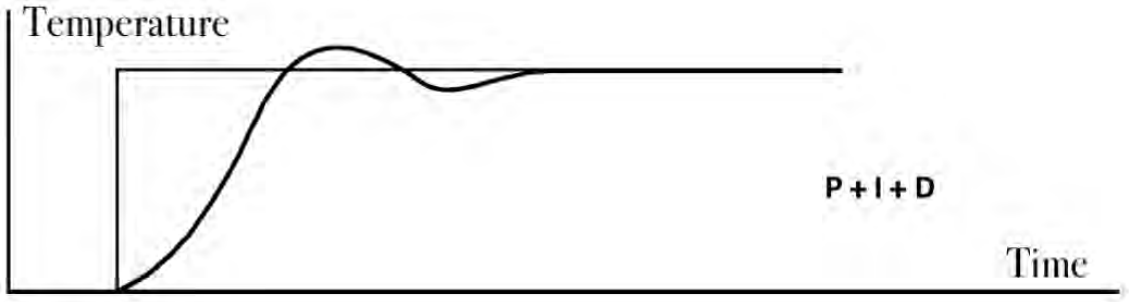

FIG. 17: A plot of temperature against time demonstrating PID control using proportional (P), integral (I) and derivative (D) settings. Proportional affects the response of a controller to an error from the setpoint, integral is proportional to the duration of the error and derivative acts on the change of the error with time.

The Lakeshore 335 temperature controller [10] comes with an autotuning function which can automate the entire tuning process except the most important step: selecting an appropriate heater range. Without a good initial estimate of the heater range, manual output and P setting, the autotune process is incredibly time consuming with a high probability of failure. Manually tuning the PID control worked best for our experimental system since the thermal mass is small and the heater should not have issues with ramping up to the setpoint temperature; thus the bulk of the tuning rested almost entirely on selecting an appropriate heater range and P value. Initial tests revealed a characteristic overshoot before accurate PID parameters which reduced at the higher limit of the heater range.

For the experimental system (Lakeshore 335 controller, platinum RTD temperature sensor and 25Ω, 100W cartridge heater), the appropriate initial settings were found to be at $P =$

$250, I = 25$, with a temperature stable at $+0.6K$ of the temperature setpoint under ambient conditions without the shielding of the furnace on and a vacuum. To obtain a temperature control within a reasonable confidence level, the same tuning had to be applied within a state as close to experimental conditions as possible.

Under initial experimental conditions, the feedback reading from the temperature sensor was $+2.3K$ compared to the setpoint. Although this offset was non-ideal, it was considered reasonable taking into account that the temperature was held constant at each step change albeit it demonstrated signs of overshoot.

EXPERIMENTAL PROCEDURE

X-Ray Diffraction Measurements (XRD)

X-ray Diffractometer

The X-ray diffractometer in the laboratory is a four circle diffractometer. The four circle element refers to the four angles (ϕ, χ, 2θ, θ) that can be used to manipulate and access different orientations during an XRD measurement. In this diffractometer, a silver (Ag) elemental source is used to produce X-rays and a 2D area detector is used to observe photons scattered in a conic section (geometry is shown in Fig. 24 and Fig. 20).

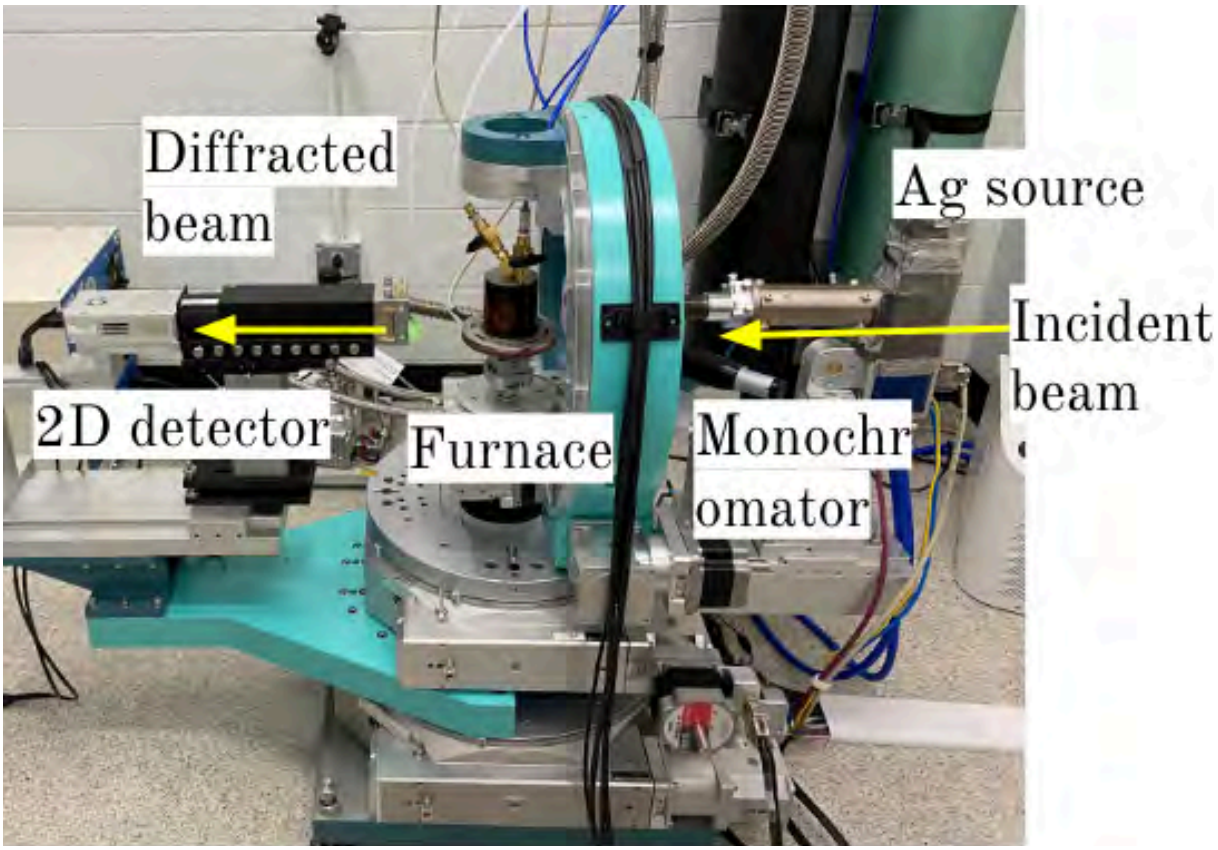

FIG. 18: Photograph of X-ray diffractometer in experimental setup. The directions of incident and diffracted beams are indicated by yellow arrow. An incident beam emitted by the Ag elemental source is passed through a monochromator and strikes the sample in the furnace. As a result, the diffracted beam is detected by the 2D detector and produces detector images.

Sample Selection and Mounting

The initial criteria (which can be determined by eye) for selecting a good sample are as follows. We select crystals that are thick, flat, and have well defined edges. Due to the color of the $CrCl_0.75Br_2.25$ crystals, it is easy to see when a crystal is thin or thick from the color of the crystals. A light colored crystal would imply a very thin layer of crystal, whereas a dark colored crystal implied a thick stacked crystal made of many layers. A thicker crystal would typically have a higher intensity when used as a sample for XRD measurements. Additionally, the flatness of a crystal is also an important criterion. A flat, uniform crystal would be easier to align and ensure higher precision when it is rotated from different sides to produce different orientations on the crystal. A crystal with uneven surfaces or curved would make it hard for the source to hit the same spot on the crystal when it is rotated through various angles.

Once a crystal has been selected, a small amount of GE varnish is used to mount the sample unto the copper post (Fig. 19). The selection of the varnish had to take into account properties that were ideal for both high and low temperature measurements: the Lakeshore VGE-7031 varnish is used as it can be used under vacuum conditions (the cryostat is placed under vacuum for low temperature measurements) and up to 470K for 2 hours. It also enhances thermal contact between the sample and the copper mount, which is important for high temperature measurements.

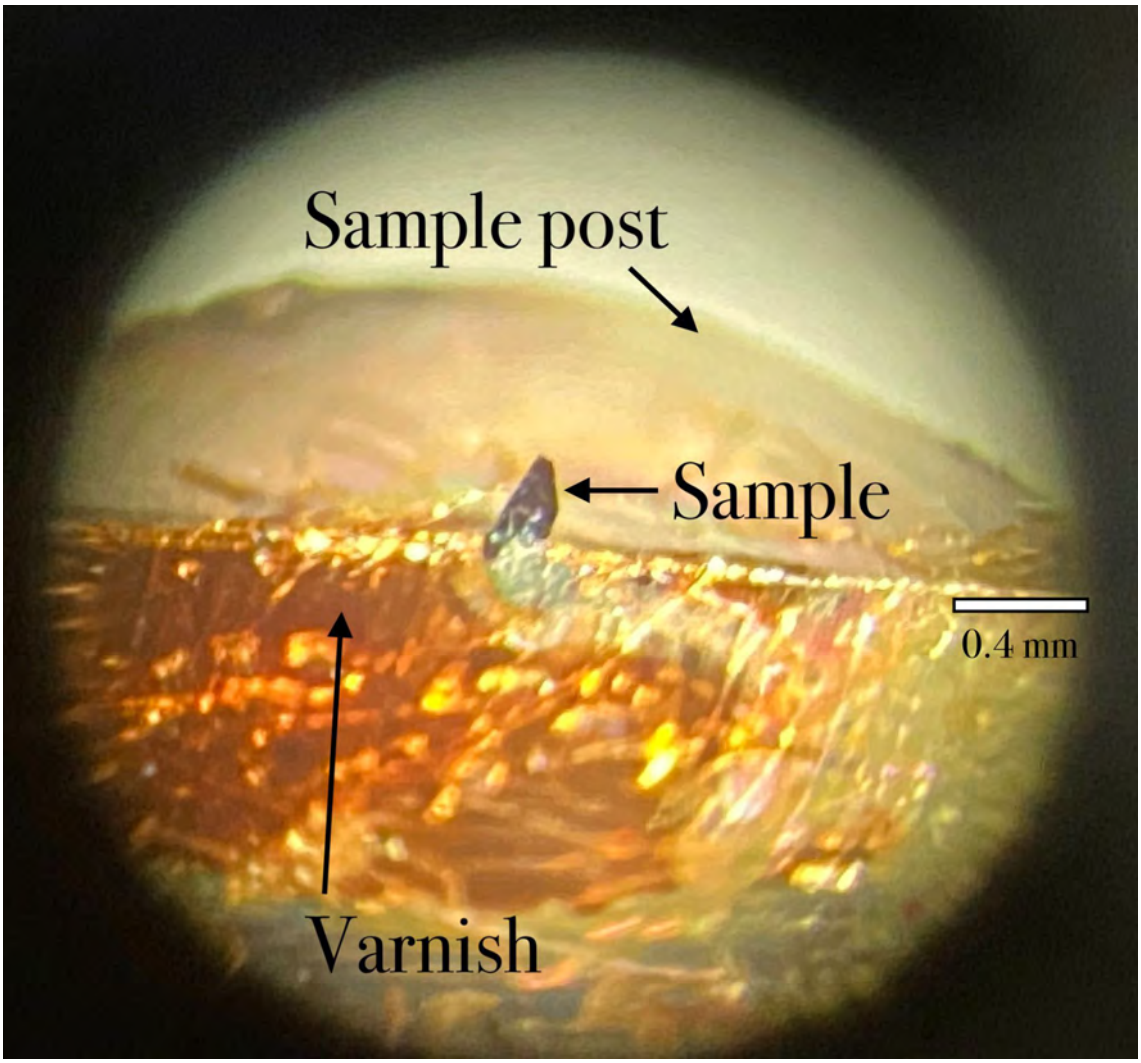

FIG. 19: A $CrCl_0.75Br_{2.25}$ sample mounted on the copper post using evaporated GE varnish solvent. The size of a single crystal is roughly on the order of a tenth of a millimeter.

As the varnish solvent evaporates quickly under room conditions, the transfer process has to be done efficiently. It is also crucial to use a soft, pointed stick for the mounting process - the wooden section of a cotton swab works well for this purpose. When broken into half, the soft, pointed surface is used to dab a small amount of the varnish unto the copper post and then to transfer the sample from the boat to the copper post. The soft surface ensures that the brittle, weakly bonded van der Waals crystal is not damaged in the process.

Once the crystal is mounted, preliminary measurements are carried out to find the Bragg peaks of interest. In this case we are interested in looking for $00l$ type peaks. The first peak we look for is the 001 peak as it has a low 2θ value and the highest intensity compared to the other known Bragg peaks; thus making it the easiest first check of the quality of the

crystal. Once the crystal is mounted in the orientation of interest, it should only require a slight rotation in the ϕ direction for the 001 peak to be observed.

Once the peak is observed, ϕ scans are run to determine the quality of the Bragg peak (Fig. 20). In a ϕ scan, the 2θ position of the crystal is fixed and scans in small *phi* steps are made within the interval of interest. The 2θ position is related to ϕ through the radius of rotation (Fig. 20). The ϕ scan provides insight on crystalline quality: data from a powder sample (Fig. 21a) appears as rings, a single crystal as dots (Fig. 21b) and data from a sample with texture somewhere in-between these extremes will appear as partial rings.

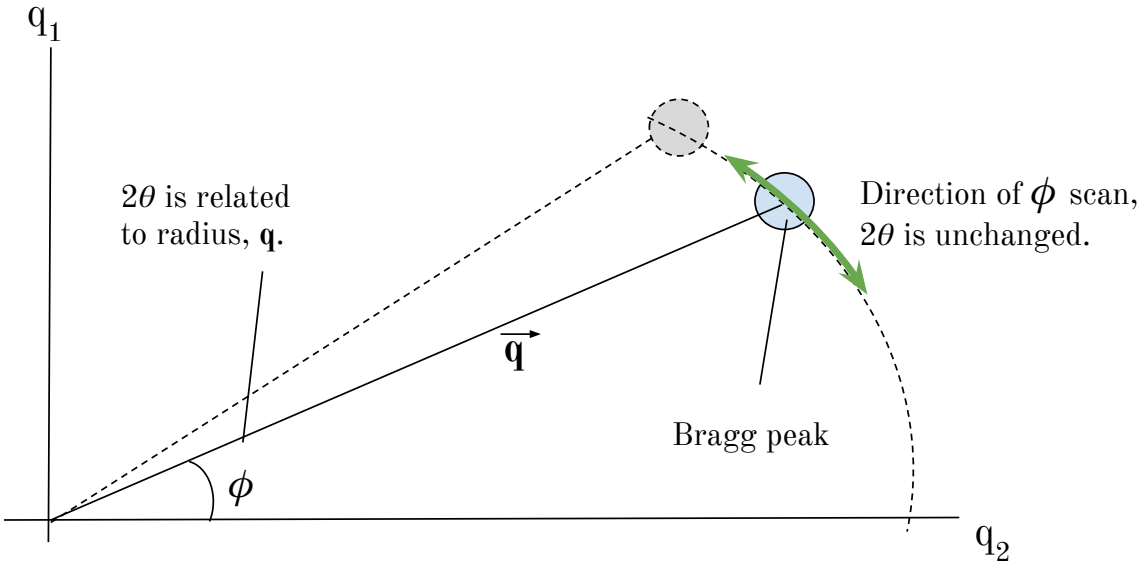

FIG. 20: Geometry of ϕ scan in momentum space. At fixed 2θ values, XRD measurements are made along the ϕ axis to monitor the changes in 2θ across a range of temperatures. ϕ scan measurements are also a test of crystalline quality.

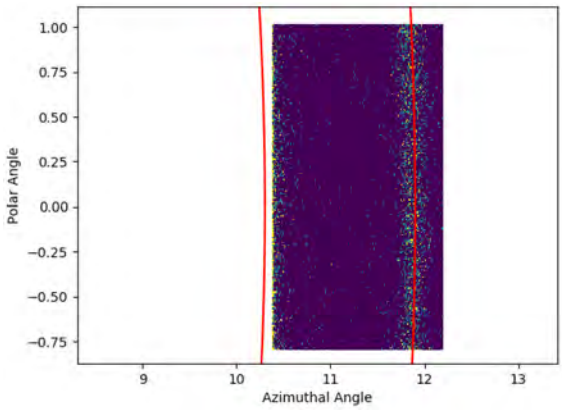

(a) Data from a powder sample of CeO_2 used to calibrate the position of the 2D detector on the diffractometer. The 2D detector image reveals powder rings as expected from a powder sample. The axes of polar and azimuthal is related to the transformation between 2D detector pixel position and the 2θ position of the sample. The red lines are markers of where the Bragg peaks of a powdered sample should appear.

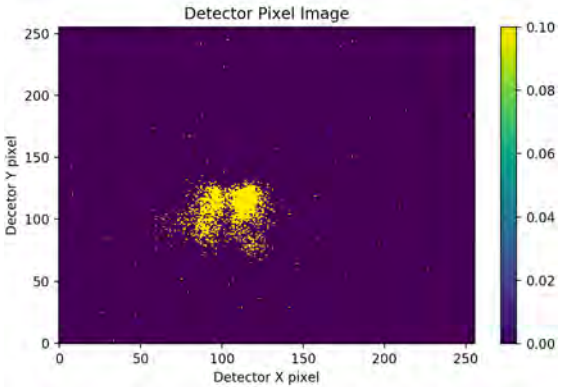

(b) Data from a single crystal sample of $CrCl_{0.75}Br_{2.25}$. The 001 Bragg peak was measured as an initial test of crystalline quality before the crystal is determined fit for use of further temperature dependent Bragg peak measurements.

FIG. 21: Data from phi scans of powdered sample (21a) and single crystal sample(21b).

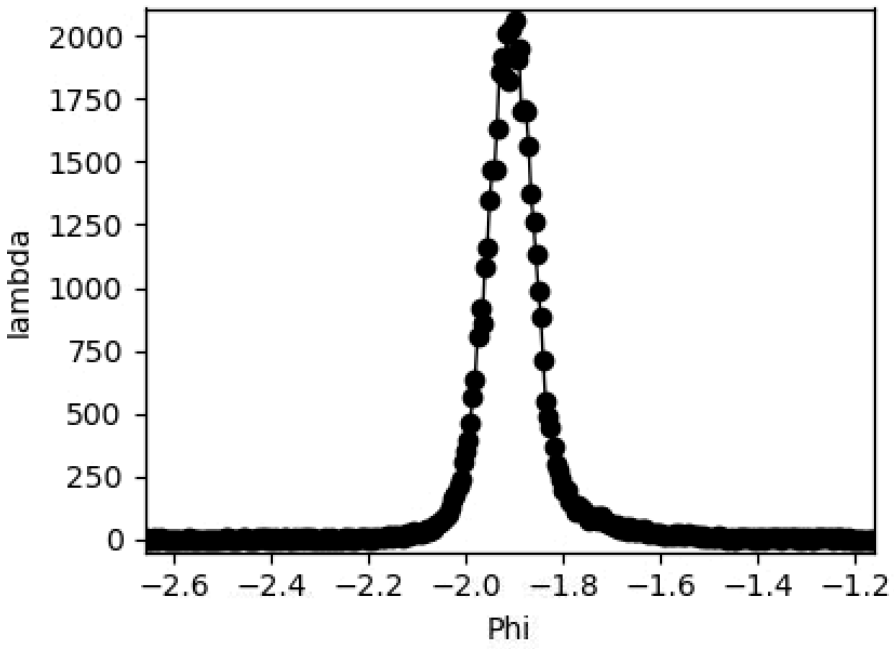

FIG. 22: At a fixed 2θ value, detector scans are made at each step of a changing ϕ. Lambda refers to the detector count of arriving photons.

The 2D area detector in the lab is especially useful for its efficiency in imaging peaks. With a 2D detector, a full image of the diffraction pattern can be taken, which is more effective compared to the multiple XRD scans that would have to be taken by a point detector or 1D detector. A ϕ scan on a sample also provides insight to the texture and quality of the sample. When single crystal samples are used for our XRD measurements, a good peak would result in detector images such as Fig. 21b. Other indicators are a strong intensity (detector counts on the order of thousands), a small FWHM (approximately around 0.2) for a phi scan and a sharp singular peak (Fig.22), rather than a noisy looking peak (which might indicate layers that are unevenly stacked such as in Fig. 23). In other words, we are looking for single peaks rather than a powder ring (Fig. 21a) or anything else in between. The observation of a good 001 peak is an important initial step for the experiment as it directly affects the quality of additional Bragg peak measurements.

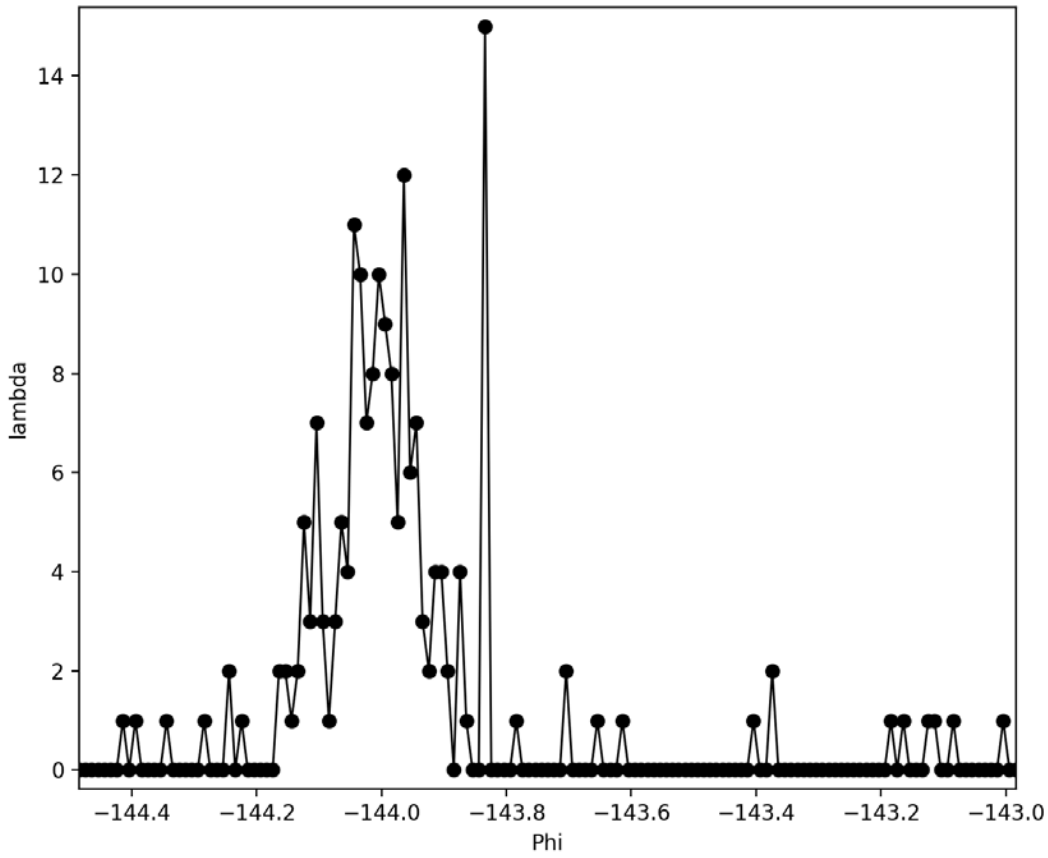

FIG. 23: Data of a ϕ scan with poor quality. The Bragg peak appears rather broad, the detector count (lambda) is low, and the shape of the peak is noisy with fluctuations rather than sharply defined as in Fig. 22.

For each temperature dependent XRD measurement, selecting, mounting and checking the quality of the crystal can take between a few hours to one day. While the process of selecting, mounting, and determining the quality of a good crystal can be arduous and time consuming, it is nonetheless one of the most important initial steps for the rest of the experiment.

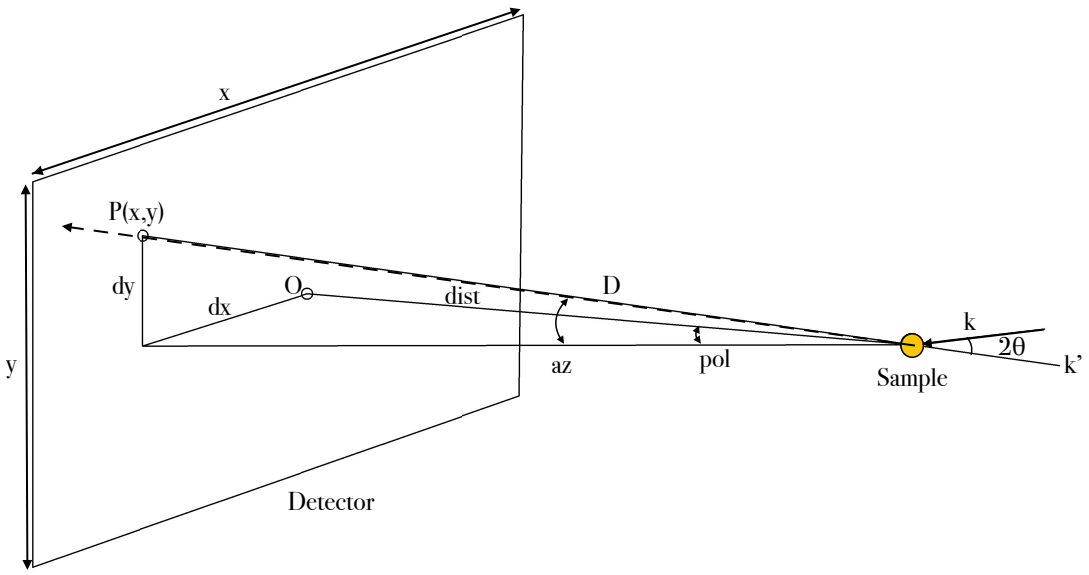

FIG. 24: Illustration of coordinate transformation relating pixel position (x,y) on 2D detector to 2θ value of crystal. (x,y) coordinates are related (pol, az) angles and finally to 2θ. The incoming beam, **k** is shown to strike the sample and outgoing beam **k'** lies along the direction of D, the distance between sample and pixel position, striking the detector. O is the centre of the detector screen.

The data analysis process begins with a detector image (Fig. 21b) of a peak of interest. In this thesis, the peak I focused on was the 005 peak as it lies along a larger **q** value and would have a more accurate 2θ value. From a detector image, the next step is to bin the counts of a pixel located at (x,y) position of the 2D area detector according to the corresponding 2θ value. For this, a relationship between the pixel position on the detector screen and the 2θ (position between **k** and $\mathbf{k}'$) has to be established.

An illustration for the relationship between pixel and crystal 2θ position is shown in Fig. 24. The main equations for relating pixel (x,y) position to (pol, az) angles are as follows.

$$az = \arctan(\frac{dy}{D}) \tag{20}$$

$$pol = \arctan(\frac{dx}{dist}) \tag{21}$$

where $D = \sqrt{dx^2 + dis^2}$ is the distance between the sample and the pixel position on the detector screen as well as the direction of $\mathbf{k}'$ and $dist$ is the distance between the sample and the origin position of the detector screen. Finally, to calculate the 2θ position corresponding to each pixel position, we use the following equation:

$$2\theta = 2\arcsin\sqrt{\frac{2 - 2\cos(pol)\cos(az)}{2}} \tag{22}$$

Since each pixel is related to the 2θ position, the counts measured by the pixel can then be separated into corresponding 2θ bins. Finally, for each ϕ step in the ϕ scan, a detector image is taken. Therefore, for a full picture of a ϕ scan at a fixed 2θ value, multiple ϕ step frames are stacked together during the reduction process (Fig. 25).

Once the counts are binned and the detector images are reduced, each temperature step can be summarized with a 2θ count plot (Fig. 26). Gaussian curves are then fitted to the figure to track the changes in the 2θ value for a peak, which will further enable analysis in d-spacing, peak width etc. In Fig. 26, there are two closely separated Bragg peaks as the X-ray emission from the source can be seen as a doublet emission $K\alpha_1 = 0.56381\mathring{A}$ and $K\alpha_2 = 0.55942\mathring{A}$ at high resolutions due to the splitting of energy levels. Error bars are also added at this stage to assess the fit of the data points to the Gaussian curve, which will be further discussed in the next section.

Error Analysis

The diffractometer has an 2D area detector: it detects the arrival of photons along a screen made up of 256×256 number of pixels: 256 along the x direction and 256 along the y direction. In other words, it measures the number of photons that arrive at those pixels within a fixed time window. As it is essentially a counting process, the arrival of photons can be treated as a Poisson process and described accordingly. The distribution of

the photons can be modelled such that the count of the detector is measuring the probability of a photon arriving ($P(A)$) or the photon not arriving ($P(!A)$) at each pixel. Following the Poisson model, the error on each individual pixel is the standard deviation of the distribution σ, i.e. $\sigma = \sqrt{I_{tot}}$, where I_{tot}, the total intensity, is the number of counts recorded by the detector corresponding to each 2θ bin.

Additionally, as the ϕ scans of a 2θ bin are stacked during the reduction process (Fig. 25), the stacking of frames are taken into account when propagating the error, ϵ for a data point corresponding to a 2θ value:

$$\epsilon = \frac{\sqrt{I_{tot}}}{N} \tag{23}$$

where N is the total number of ϕ steps in the corresponding 2θ bin.

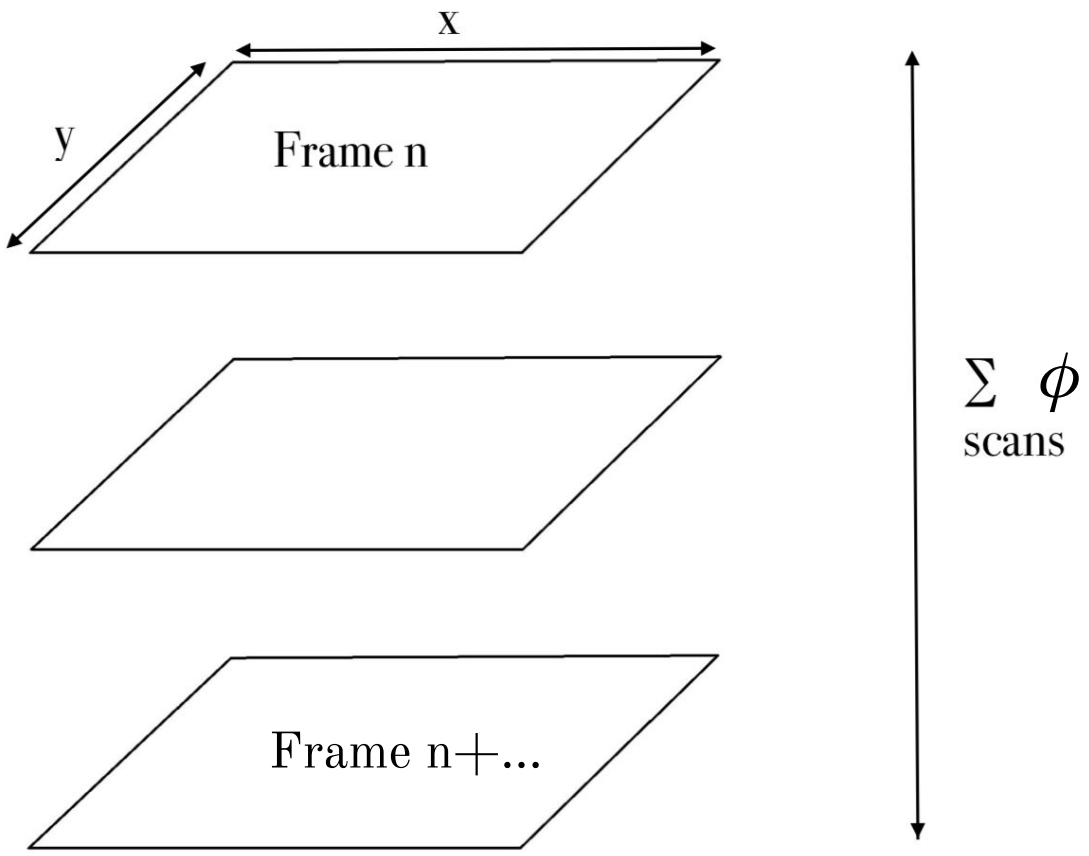

FIG. 25: At a fixed 2θ value, detector frames are taken at each step of a changing ϕ value. Multiple detector frames are then stacked to form a reduced image by the process of binning counts according to 2θ values.

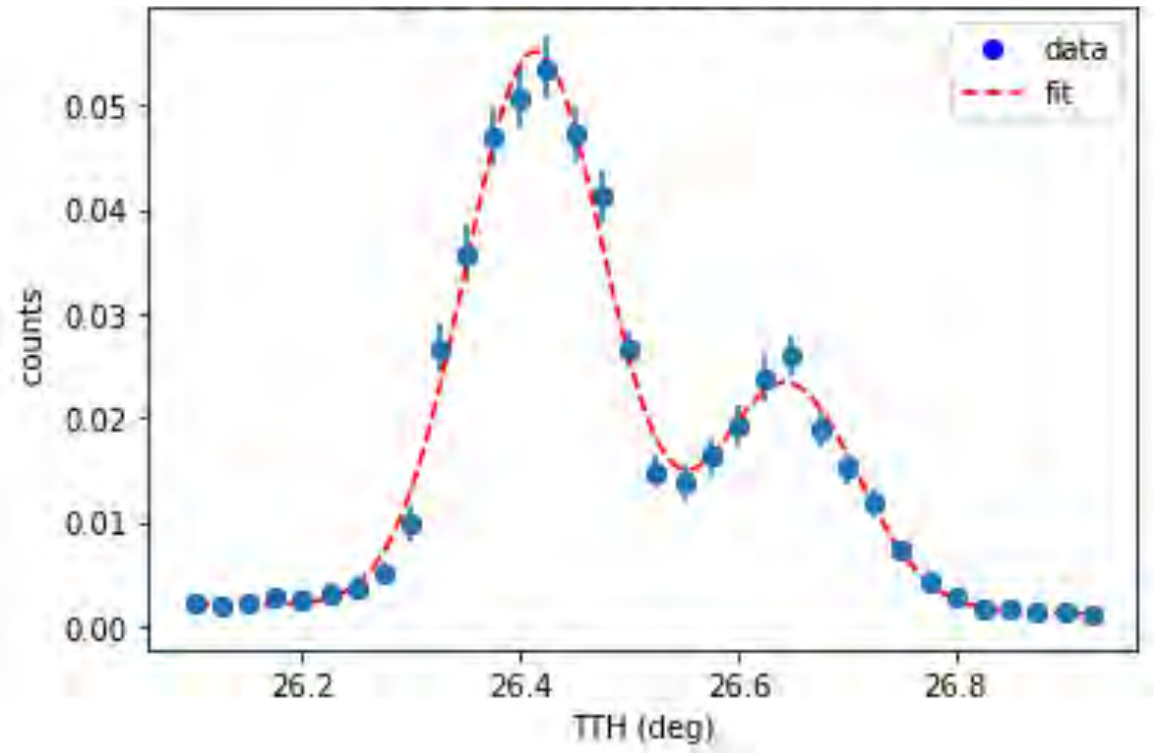

FIG. 26: Plot of counts binned according to 2θ values, a Gaussian fit is then applied to the data points and to fit the Bragg peak of interest. Error bars are added by dividing the square root of the counts by number of frames in a 2θ bin. The two closely separated Bragg peaks are seen as the X-ray emission from the source can be seen as a doublet emission $K\alpha_1$ and $K\alpha_2$ at high resolutions due to the splitting of energy levels.

RESULTS AND ANALYSIS

To examine the variation of the crystal structure in $CrCl_xBr_{3-x}$ with temperature and in particular to identify any structural phase transitions, 22KeV X-ray diffraction in transmission geometry of the bulk crystals was measured between 220 to 420 K. The measurements from $300 - 420$K were done using the furnace and measurements below 310K were taken using the cryostat in the lab. Data were collected in 1 K increments with an average temperature sweep rate of 1 K/min. At each temperature increment, 3 minutes were allocated for the cryostat to stabilize in temperature and 5 minutes for the furnace before a high resolution ϕ scan in 2θ was made.

The 005 reflection from a $CrCl_{0.75}Br_{2.25}$ crystal was measured as the temperature was varied (Fig. 27), revealing a discontinuity in the 2θ value of the 005 peak near 300K. The discontinuity of the 2θ value (highlighted on the plot) suggests that a temperature-induced structural transition has occurred in $CrCl_{0.75}Br_{2.25}$ at around room temperature. The same pattern is seen in the contour plot of intensity against diffraction angle and temperature in Fig. 28 [4]. As $CrCl_3$ undergoes the same structural transition at 240K and $CrBr_3$ at 420K, a structural transition temperature of approximately 300K for $CrCl_{0.75}Br_{2.25}$ is reasonable, given that the mixed compound lies within two ends of the series.

Interestingly, the temperature region of around (300 ± 5)K is accessible when either the cryostat or the furnace is used for XRD measurements. In other words, it is expected that the data points would overlap the way the beginning of each data set overlaps from $220 - 300$K. However, this is not the case in Fig. 27. Some possible reasons for this include uncertainties in the sample position and temperature. $CrCl_{0.75}Br_{2.25}$ crystals are made of many weakly bonded layers and their Bragg peaks are very sensitive to crystal position. Additionally, the position of temperature sensor for the furnace is not as close to the sample as is the cryostat, since by design of the furnace, the temperature sensor is positioned closer to the furnace than the sample to assist the heating process. As the temperature changes in the cryostat and furnace, thermal expansion in the sample post could cause a change the sample position as measured by the XRD.

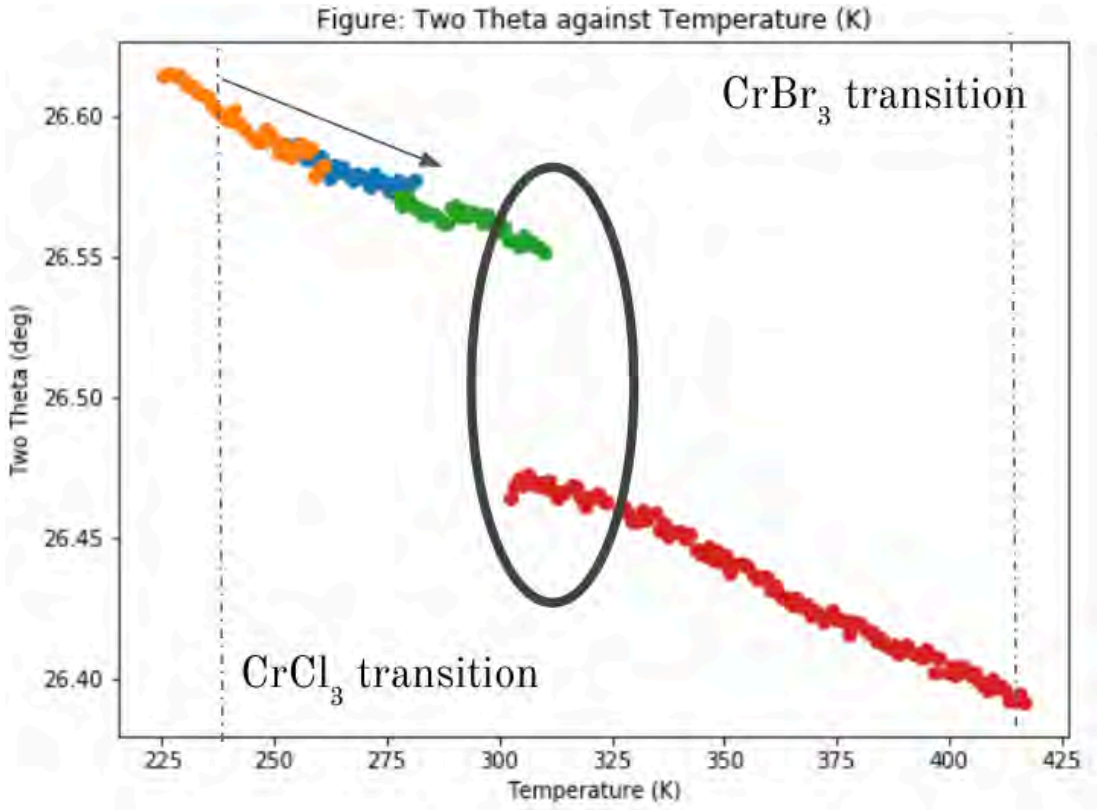

FIG. 27: Plot of 2θ values against temperature showing 005 peak reflection in a $CrCl_{0.75}Br_{2.25}$ single crystal on a warming cycle. A set of coloured data points indicate a continuous set of measurement across the temperature range. Measurements were taken during a warming cycle; one set of colored data points indicate a single continuous measurement cycle.

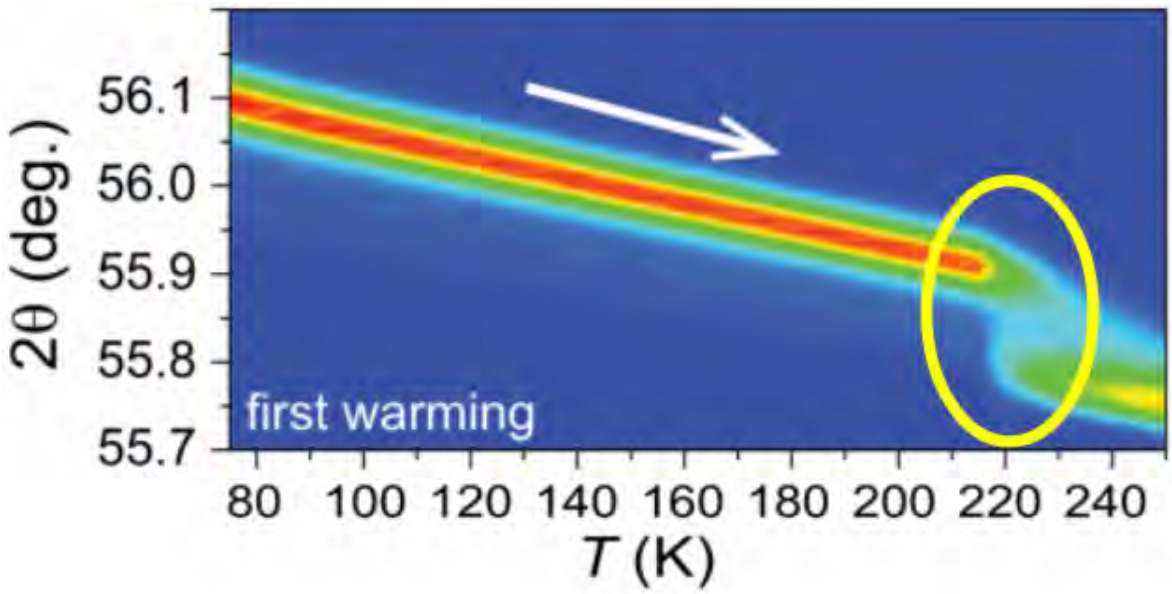

FIG. 28: Contour plot of intensity versus diffraction angle and temperature showing the monoclinic 004 reflection measured from a CrI_3 single crystal on a warming cycle. [4]

For this, various alignment steps can improve the accuracy of the sample position, i.e. using a standard alignment sample (such as the 111 peak of a Si sample or the CeO_2 sample) to ensure that the centre of rotation is the same for both the cryostat and furnace setup before measuring the $CrCl_{0.75}Br_{2.25}$ sample. Ideally, the centre of rotation alignment would be done as frequently as is possible. However, it is difficult to switch out samples at small temperature increments as making measurements in the cryostat involves pumping down to vacuum conditions, whereas switching out samples when the furnace and sample post are at high temperatures would also be tricky. A compromise in this case could be to make measurements across a shorter continuous temperature range and to align at the beginning of each round of measurement, equivalent to more frequent alignments at each temperature range.

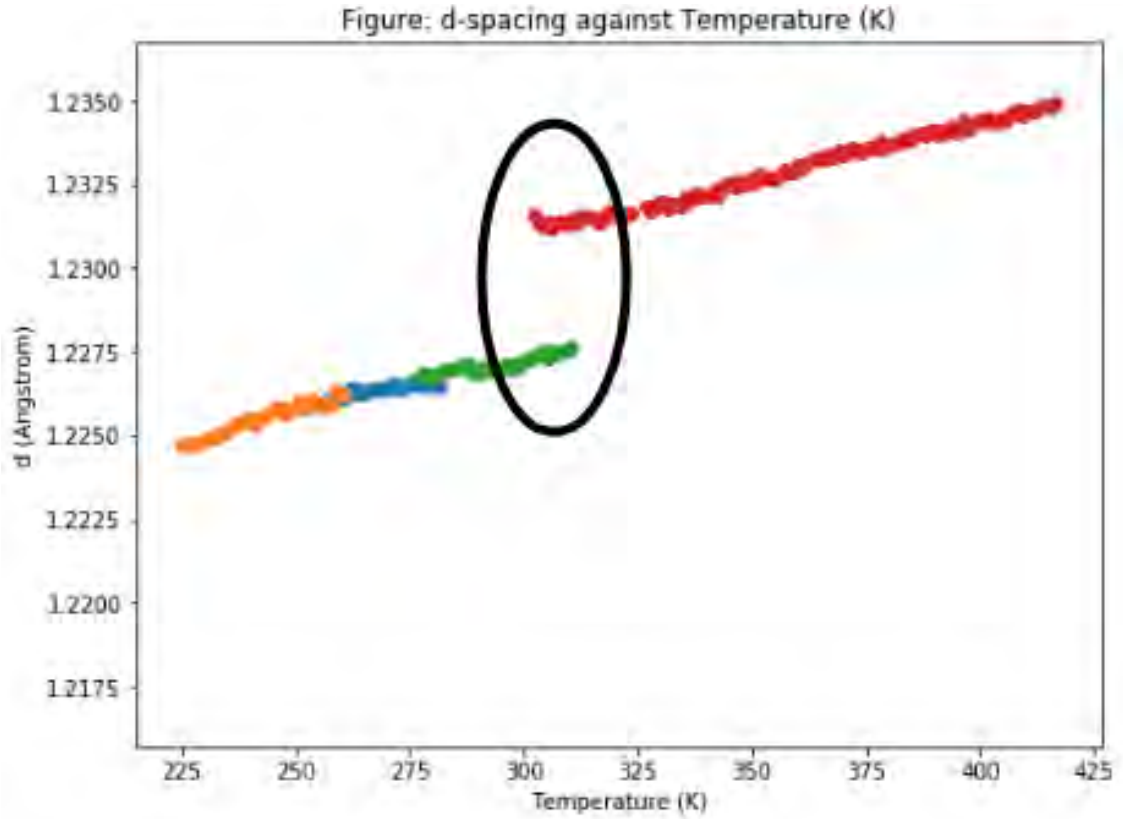

FIG. 29: Plot of d layer spacing values against temperature from 005 peak measurement in $CrCl_{0.75}Br_{2.25}$ sample showing temperature dependence of the spacing (d) between crystal layers determined from XRD measurements during a warming cycle.

From similar measurements of the $CrCl_{0.75}Br_{2.25}$ crystal, d-spacing is plotted against temperature in Fig. 29, with the coexistence region highlighted on the plot. Experimental

results from the $CrCl_{0.75}Br_{2.25}$ again demonstrate a similar pattern when compared to literature: the same coexistence region of two structure exists in the plot for experimental data and literature (Fig. 30).

Further analysis is needed to fully understand the experimental data and confirm the structural transition at 300K. For example, a detailed plot of peak width against temperature would reveal changes in the 005 peak: any signs of broadening or increase in the number of peak at the site would further confirm the structural transition. Additional comparisons with literature values for the slope in temperature-dependent 2θ and d spacing plots, as well as comparison with literature Debye-Waller factors and thermal expansion coefficients would give further information on the change in lattice parameters across different temperatures.

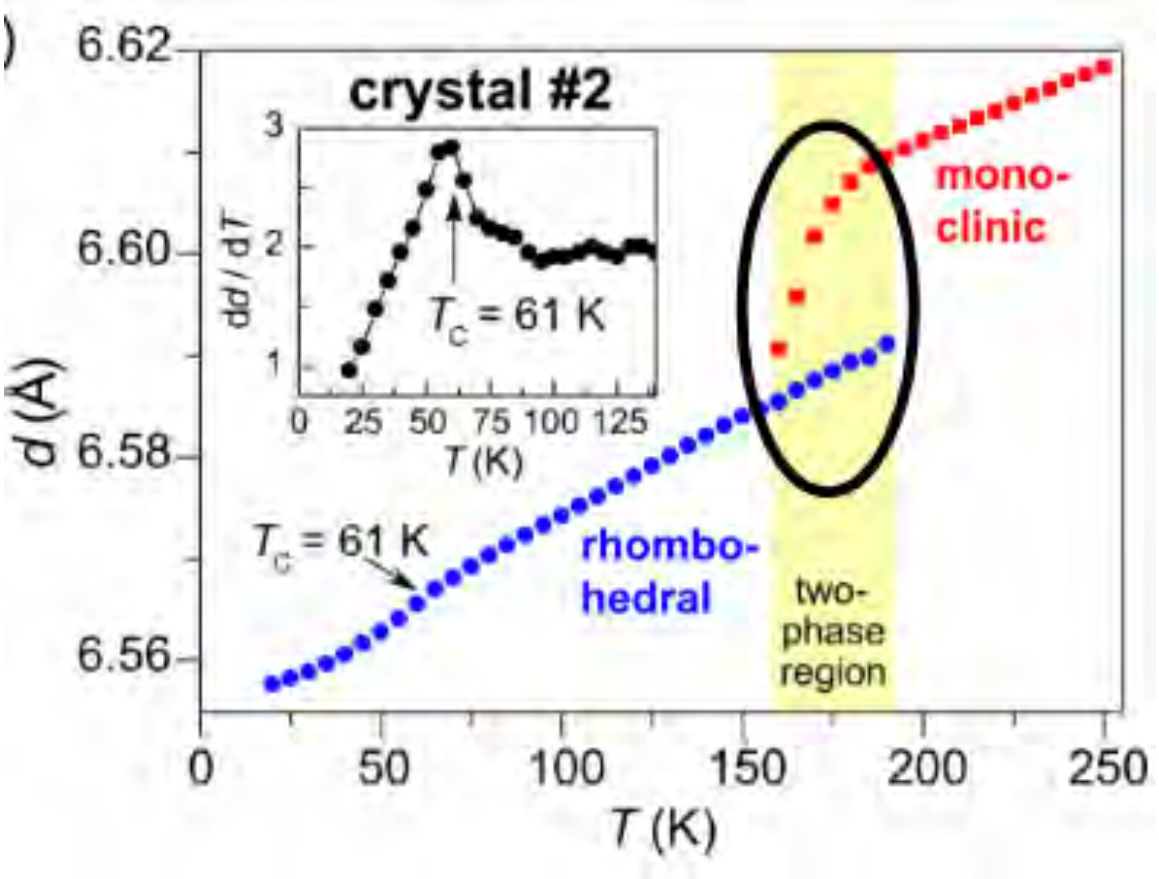

FIG. 30: Temperature dependence of d spacing between CrI_3 layers determined from XRD measurements upon cooling after the cycling through the phase transition once. [4]

CONCLUSION

In this thesis, I achieved preliminary confirmation of a a single structural transition in mixed chromium trihalides $CrCl_{3-x}Br_x$ at approximately 300K was achieved, as demonstrated in Fig. 27 and Fig. 29 with comparison to ongoing research. This is among the first steps of ruling out phase inhomogeneity in a mixed chromium trihalide compound in the research of tuning magnetic anisotropy by mixing lighter and heavier halides. Ruling out phase inhomogeneity will allow us to rule out the existence of different domains of hard and easy axis in mixed chromium trihalide compounds - this clarifies the main result (Fig. 9) of tuning magnetic anisotropy from [2] with average magnetization measurements. Additionally, a furnace-shielding-stage assembly for high temperature X-ray diffraction measurements was successfully designed and constructed. Apart from its usage for this thesis, the furnace can be used for temperatures up to $\approx 400°C$ with further improvements for heat retention as well as insulation for connecting components. Once the location of the temperature sensor is moved closer to the sample, greater accuracy for temperature-dependent measurements can also be achieved.

In order to make progress and fully rule out phase inhomogeneity in mixed chromium trihalide compounds and in particular $CrCl_{3-x}Br_x$, future measurements should focus on XRD measurements of the 005 Bragg peak in different samples of the same Br content x as well as new samples of different x values. Furthermore, XRD measurements can be made along different warming and cooling cycles to examine the corresponding thermal hysteresis responses in the compound - this will provide more information on temperature-induced structural transitions that occur.

Summary of Thesis Achievements

In this thesis, I achieved:

- the preliminary confirmation of a single structural transition in mixed chromium trihalides $CrCl_{3-x}Br_x$ at approximately 300K, ruling out phase inhomogeneity in a mixed compound, and
- the construction of a furnace-shielding-stage assembly for high temperature X-ray diffraction measurements.

Directions for Future Work

Suggestions for future measurements to fully rule out phase inhomogeneity in mixed chromium trihalide compounds include:

- performing XRD measurements of 005 Bragg peak of different samples of same Br content x,
- performing XRD measurements of 005 Bragg peak at different Br content values x,
- performing XRD measurements along different warming and cooling cycles to examine various thermal hysteresis responses in mixed chromium trihalides $CrCl_{3-x}Br_x$, and
- moving the location of temperature sensor in the furnace closer to the sample to improve the accuracy in temperature measurements.

[1] Clark G. Navarro-Moratalla E. et al. Huang, B. Layer-dependent ferromagnetism in a van der waals crystal down to the monolayer limit. *Nature*, 546:270–273, 2017.

[2] M; et. al. Abramcuk. Controlling magnetic and optical properties of the van der waals crystal $CrCl_{3-x}Br_x$ via mixed halide chemistry. *Adv. Mat.*, 30, 2018.

[3] Christopher Hammond. *The basics of crystallography and diffraction*. Oxford University Press, Oxford University Press Inc, New York, third edition, 2009.

[4] H.; Cooper-V.R.; Sales B.C McGuire, M.A.; Dixit. Coupling of crystal structure and magnetism in the layered, ferromagnetic insulator CrI_3. *Chem. Mater*, 27:612–620, 2015.

[5] Stephen Blundell. *Magnetism in Condensed Matter*. Oxford University Press, Oxford University Press Inc, New York, first edition, 2001.

[6] Yuval Orweg. *Concepts of Condensed Matter*. 2016.

[7] Y. Kawazoe P. Jena. J. Liu, Q. Sun. Exfoliating biocompatible ferromagnetic cr-trihalide monolayers. *Phys. Chem. Chem. Phys.*, 18:8777, 2016.

[8] P. Zhu C.-H. Lam J. W.-B. Zhang, Q. Qu. Robust intrinsic ferromagnetism and half semiconductivity in stable two-dimensional single-layer chromium trihalides. *Mater. Chem. C.*, 48: 12457, 2015.

[9] J. Fernandez-Rossier J. L. Lado. On the origin of magnetic anisotropy in two dimensional CrI_3. *2D Materials*, 4:3, 2017.

[10] *User's Manual Model 335 Temperature Controller*, July 2017.

[11] J. Bland. *A Mössbauer Spectometry and Magnetometry Study of Magnetic Multilayers and Oxides*. Ph.D. thesis, University of Liverpool, 2002.

[12] H. Kamimura J. F. Dillon, JR. and J. P. Remeika. Magneto-optical properties of ferromagnetic chromium trihalides. *J. Phys. Chem. Solids*, 27:1531–1549, 1966.